

1 **Mass-spectrometry-based draft of the Arabidopsis proteome**

2 **Julia Mergner<sup>1</sup>, Martin Frejno<sup>1</sup>, Markus List<sup>2</sup>, Michael Papacek<sup>3</sup>, Xia Chen<sup>4</sup>, Ajeet**  
3 **Chaudhary<sup>4</sup>, Patroklos Samaras<sup>1</sup>, Sandra Richter<sup>5</sup>, Hiromasa Shikata<sup>6,7</sup>, Maxim Messerer<sup>8</sup>,**  
4 **Daniel Lang<sup>8</sup>, Stefan Altmann<sup>9</sup>, Philipp Cyprys<sup>10</sup>, Daniel P. Zolg<sup>1</sup>, Toby Mathieson<sup>11</sup>,**  
5 **Marcus Bantscheff<sup>11</sup>, Rashmi R. Hazarika<sup>12,13</sup>, Tobias Schmidt<sup>1</sup>, Corinna Dawid<sup>14</sup>, Andreas**  
6 **Dunkel<sup>14</sup>, Thomas Hofmann<sup>14</sup>, Stefanie Sprunck<sup>10</sup>, Pascal Falter-Braun<sup>9,15</sup>, Frank**  
7 **Johannes<sup>12,13</sup>, Klaus F. X. Mayer<sup>8,16</sup>, Gerd Jürgens<sup>5</sup>, Mathias Wilhelm<sup>1</sup>, Jan Baumbach<sup>2</sup>,**  
8 **Erwin Grill<sup>3</sup>, Kay Schneitz<sup>4</sup>, Claus Schwechheimer<sup>6</sup> and Bernhard Kuster<sup>1,13,17</sup> \***

9 <sup>1</sup>*Chair of Proteomics and Bioanalytics, Technical University of Munich (TUM), Freising,*  
10 *Germany*

11 <sup>2</sup>*Chair of Experimental Bioinformatics, Technical University of Munich (TUM), Freising, Germany*

12 <sup>3</sup>*Chair of Botany, Technical University of Munich (TUM), Freising, Germany*

13 <sup>4</sup>*Plant Developmental Biology, Technical University of Munich (TUM), Freising, Germany*

14 <sup>5</sup>*Center for Plant Molecular Biology, University of Tübingen, Tübingen, Germany*

15 <sup>6</sup>*Chair of Plant Systems Biology, Technical University of Munich (TUM), Freising, Germany*

16 <sup>7</sup>*Division of Plant Environmental Responses, National Institute for Basic Biology, Okazaki,*  
17 *Japan*

18 <sup>8</sup>*Plant Genome and Systems Biology, Helmholtz Center Munich, German Research Center for*  
19 *Environmental Health, Munich-Neuherberg, Germany*

20 <sup>9</sup>*Institute of Network Biology (INET), Helmholtz Center Munich, German Research Center for*  
21 *Environmental Health, Munich-Neuherberg, Germany*

22 <sup>10</sup>*Cell Biology and Plant Biochemistry, University of Regensburg, Regensburg, Germany*

23 <sup>11</sup>*Cellzome GmbH, Heidelberg, Germany*

24 <sup>12</sup>*Population epigenetics and epigenomics, Technical University of Munich (TUM), Freising,*  
25 *Germany*

26 <sup>13</sup>*Institute of Advanced Study (IAS), Technical University of Munich (TUM), Freising, Germany*

27 <sup>14</sup>*Chair of Food Chemistry and Molecular Sensory Science, Technical University of Munich*  
28 *(TUM), Freising, Germany*

29 <sup>15</sup>*Chair of Microbe-Host Interactions, Ludwigs-Maximilians-University (LMU), Munich, Germany*

30 <sup>16</sup>*Plant Genome Biology, Technical University of Munich (TUM), Freising, Germany*

31 <sup>17</sup>*Bavarian Biomolecular Mass Spectrometry Center (BayBioMS), TUM, Freising, Germany*

32 **Abstract**

33 Plants are indispensable for life on earth and represent organisms of extreme biological  
34 diversity with unique molecular capabilities <sup>1</sup>. Here, we present a quantitative atlas of the  
35 transcriptomes, proteomes and phosphoproteomes of 30 tissues of the model plant *Arabidopsis*

36 *thaliana*. It provides initial answers to how many genes exist as proteins (>18,000), where they  
37 are expressed, in which approximate quantities (>6 orders of magnitude dynamic range) and to  
38 what extent they are phosphorylated (>43,000 sites). We present examples for how the data  
39 may be used, for instance, to discover proteins translated from short open reading frames, to  
40 uncover sequence motifs involved in protein expression regulation, to identify tissue-specific  
41 protein complexes or phosphorylation-mediated signaling events to name a few. Interactive  
42 access to this unique resource for the plant community is provided via ProteomicsDB and  
43 ATHENA which include powerful bioinformatics tools to explore and characterize Arabidopsis  
44 proteins, their modifications and interplay.

#### 45 **Main**

46 The plant model organism *Arabidopsis thaliana* (AT) has revolutionized our understanding of  
47 plant biology and influenced many other areas of the life sciences <sup>1</sup>. Knowledge derived from  
48 Arabidopsis has also provided mechanistic understanding of important agronomic traits in crop  
49 species <sup>2</sup>. The Arabidopsis genome was sequenced 20 years ago and hundreds of natural  
50 variants have since been analyzed at the genome and epigenome level <sup>3,4</sup>. In contrast, the  
51 Arabidopsis proteome as the main executor of most biological processes is far less  
52 comprehensively characterized. To address this gap, we used state-of-the-art mass  
53 spectrometry and RNA sequencing (RNA-seq) to provide the first integrated proteomic,  
54 phosphoproteomic and transcriptomic atlas of Arabidopsis. Illustrated by selected examples, we  
55 show how this rich molecular resource can be used to explore the function of single proteins or  
56 entire pathways across multiple omics levels.

#### 57 **Multi-omics atlas of Arabidopsis**

58 We generated an expression atlas covering, on average,  $17,603 \pm 1,317$  transcripts,  
59  $14,430 \pm 911$  proteins and  $14,689 \pm 2,509$  phosphorylation sites (p-sites) per tissue, using a  
60 reproducible biochemical and analytical approach (Fig. 1a,b; Extended Data Fig. 1a-c;  
61 Supplementary Data 1,2). In total, the protein expression data covers 18,210 of the 27,655  
62 protein-coding genes (66%) annotated in Araport11 <sup>5</sup>. This is a substantial increase compared  
63 to the percentage of genes with protein level evidence reported in UniProt (27%) <sup>6</sup> and more  
64 than double the number of proteins identified in an earlier tissue proteome analysis <sup>7</sup> (Fig. 1c,  
65 Extended Data Fig. 1d-f). In addition, we report tissue-resolved quantitative evidence for a total  
66 of 43,903 p-sites making this study the most comprehensive single Arabidopsis  
67 phosphoproteome published to date (Fig. 1c). 47% of the expressed proteome was found to be  
68 phosphorylated in at least one instance, confirming earlier analyses of individual

69 phosphoproteomes or information assembled in the PhosPhAT database (Extended Data Fig.  
70 1g,h) <sup>8,9</sup>. The actual figures *in plantae* are likely considerably higher as there is limited overlap  
71 between these data sources. This can be readily explained by technical factors (e. g. insufficient  
72 sequence coverage) and, more importantly, differences in plant genotypes or stimuli that  
73 influence phosphorylation. The above figures are similar to those reported for mammalian  
74 systems, underscoring the strong conservation of protein post-translational modifications as a  
75 means to create functional diversity from a limited set of genes and proteins <sup>10</sup>.

76 The atlas can be explored using the new web portal ATHENA (Arabidopsis Thaliana ExpressioN  
77 Atlas; athena.proteomics.wzw.tum.de) and ProteomicsDB (www.proteomicsdb.org) <sup>11</sup>. Analysis  
78 and visualization options include co-expression analysis, the exploration of tissue-specific  
79 interaction networks and a tool for predicting tandem mass spectra of peptide sequences, which  
80 can be used to validate peptide identifications reported in this study <sup>12</sup> (Fig. 2a,b; Supplementary  
81 Table 1). ProteomicsDB further provides spectral libraries for >328,000 unmodified and >43,000  
82 phosphorylated peptides. These can facilitate the development of quantitative mass  
83 spectrometry-based protein assays which is particularly useful for research in Arabidopsis,  
84 where comparatively few antibodies exist.

### 85 ***Proteomic annotation of the genome***

86 Using Araport11, the proteomic data corroborated a substantial number of annotated open  
87 reading frame (ORF) borders based on the detection of 2,776 N-terminal and 2,656 C-terminal  
88 peptides (Extended Data Fig. 2a). As expected, N-terminal peptides often showed cleavage of  
89 the initiator methionine and N-terminal acetylation which was strongly dependent on the amino  
90 acid adjacent to the initiator methionine (Extended Data Fig. 2b,c) <sup>13</sup>. The MS data covered, on  
91 average, 44% of each protein sequence, enabling the detection of unique peptides for 14,115  
92 protein isoforms. In 297 cases, the data distinguished also two or three splice variants  
93 (Extended Data Fig. 2d-f; Supplementary Data 3). A selection of these isoform-specific peptides  
94 was validated using synthetic peptides (confirmation rate 80%; Extended Data Fig. 2g). To  
95 investigate the potential translation of predicted short open reading frames (sORF), we  
96 searched the proteomic data against a published and an in-house compiled sORF collection  
97 (ARA-PEP <sup>14</sup>; ATSO) leading to the identification of 51 distinct sORFs that were subsequently  
98 confirmed using synthetic peptides (Extended Data Fig. 2g,h; Supplementary Data 3). These  
99 results demonstrate the potential of the atlas to refine Arabidopsis gene models and protein  
100 sequences.

### 101 ***Quantitative expression landscapes***

102 The dynamic range of protein and transcript expression spanned six and four orders of  
103 magnitude, respectively (Extended Data Fig. 2i,j). As described before, protein evidence was  
104 underrepresented for low abundant transcripts<sup>15</sup>, indicating that proteome coverage was not yet  
105 exhaustive. Low abundant transcripts were enriched for gene ontology (GO) terms such as cell  
106 signaling or gene expression regulation (Supplementary Data 4). Still, the protein data cover  
107 ~50% of all annotated transcription factors and ~75% of all transcriptional regulators, kinases  
108 and phosphatases, many of which are themselves post-translationally regulated (Extended Data  
109 Fig. 2k)<sup>16,17</sup>. Interestingly, protein phosphorylation was detected across the entire dynamic  
110 range of protein expression, highlighting the efficiency of the employed phosphopeptide  
111 enrichment (Extended Data Fig. 2j).

112 A breakdown of the molecular data for individual tissues or morphologically similar groups (e.g.  
113 leaf, seed or root) showed that only few transcripts or proteins are expressed in a truly specific  
114 manner (Extended Data Fig. 3a). Instead, tissue types are characterized by distinct quantitative  
115 abundance patterns. For instance, the floral organs express a similar set of genes but at levels  
116 that are characteristic for each flower compartment. Here, the MADS domain transcription  
117 factors showed the expected differential expression, thus recapitulating established models of  
118 floral organ identity<sup>18</sup> (Extended Data Fig. 3b,c).

119 The strong variation in quantitative gene expression between tissue groups was evident on both  
120 protein and transcript level (Extended Data Fig. 3d,e). Still, we found surprisingly little overlap in  
121 the rank order or even identity of the most abundant proteins and mRNAs within any given  
122 tissue (Extended Data Fig. 3e,f). Extreme expression ranges were detected for e.g. seeds,  
123 where the storage protein CRA1 accounted for ~10% of the total protein and the ten most  
124 abundant gene products already represented more than 30% of the total amount of protein or  
125 transcript, respectively (Extended Data Fig. 3e,g). Similarly, the RuBisCO complex, renowned  
126 as the most abundant plant protein on earth, accounted for 4-7% of total leaf protein content<sup>19</sup>  
127 (Extended Data Fig. 3g). We note that despite the dominance of some proteins in certain  
128 tissues, we show that proteomes of plant tissues can be probed very deeply using current  
129 technology, countering the long-standing notion that plant proteomics is particularly difficult<sup>20</sup>.  
130 As expected, photosynthetic activity was one of the main factors for expression pattern  
131 variations between tissues, which can also be related to plastid localized proteins and their  
132 abundance (Extended Data Fig. 3h,i). The most divergent expression pattern on both transcript  
133 and protein level, however, was found for pollen (Extended Data Fig. 3h).

134 The comparison of expression patterns between tissues can be used to ascertain biological  
135 functions of individual proteins or to disentangle closely related protein family members. A  
136 closer look at the AGCVIII kinase family (23 members in Arabidopsis) <sup>21</sup> revealed high protein  
137 expression of members of the D6PK subfamily in embryos as well as of AGC1.5 and AGC1.7  
138 kinases in flowers and pollen (Fig. 2c). In line with these results, follow-up experiments showed  
139 promotor activity for *AGC1.5* and *AGC1.7* but not for the closely related *AGC1.6* in pollen,  
140 strongly supporting the contribution of the former two in pollen tube growth <sup>22</sup> (Fig. 2d,e). We  
141 further uncovered an important role for the D6PKs in embryo development, where a combined  
142 knockout synergistically increased the occurrence of aberrant embryo phenotypes in loss-of-  
143 function mutants (Fig. 2f-i).

#### 144 ***Regulation of protein amount in tissues***

145 The amount of protein for a given gene is determined by a regulatory system comprising  
146 anabolic and catabolic transcriptional, translational and post-translational processes. This has  
147 been extensively studied in unicellular organisms and, more recently, in human <sup>23</sup>. While this  
148 broad area of research cannot be covered in detail here, consistent observations were made in  
149 the current study. We found positive correlation between transcript and protein levels in most  
150 tissues (Pearson's *R* 0.28-0.7, Extended Data Fig. 4a), with the majority of high or low abundant  
151 transcripts resulting in high or low abundant proteins, respectively <sup>24</sup> (Fig. 3a). To identify further  
152 molecular determinants of protein abundance, we implemented a model selection approach and  
153 tested each of the selected features for the potential to explain protein level variations on a  
154 tissue-specific or global level (Extended Data Fig. 4b-e; Supplementary Data 5). In addition to  
155 well-known predictors like transcript levels and codon usage <sup>25</sup>, evolutionary conservation,  
156 mRNA sequence motifs and the number of protein interactions were significant predictors of  
157 protein levels (Fig. 3b). However, a large proportion (48%) of protein abundance variation still  
158 remains unexplained, suggesting that many additional molecular factors with great individual but  
159 lower global impact may be at work which will require careful case by case experiments to  
160 resolve.

161 Protein versus transcript abundance plots clearly show that similarly abundant transcripts often  
162 lead to proteins with >100-fold differences in abundance. These differences in the protein-to-  
163 mRNA ratio (PTR) of genes might be due to differences in translation efficiency of a given  
164 transcript, transcript stability and/or the stability of the respective protein (Fig. 3c) <sup>26</sup>. High PTRs  
165 were detected for genes involved in photosynthesis or energy metabolism (e.g. *petA* and *rbcl*)  
166 (Supplementary Data 4). This implies optimized translation and stability of those proteins (and

167 transcripts) that are needed in large quantities. Conversely, genes with low PTRs were enriched  
168 in processes such as hormone-mediated signaling pathways, which, in plants, often involve  
169 protein degradation<sup>27</sup>. Members of the auxin-labile AUX/IAA protein family (e. g. IAA8, IAA13)  
170 for example show low protein signal despite high transcript levels and are known to be under  
171 tight control of auxin-dependent proteasomal degradation<sup>28</sup> (Fig. 3a).

172 We also observed inter-tissue variation of PTRs, especially for seed and pollen (Fig. 3d). Genes  
173 with low PTRs in seeds mainly show differential abundance at the protein level and proteome-  
174 wide time-resolved measurements in germinating seeds in response to cycloheximide  
175 (translation block) or MG132 (proteasome block) treatment suggest that low PTR proteins are  
176 rapidly translated from stored mRNA upon germination. High PTR proteins do not show this  
177 behavior implying that they are stored in seed to be readily available for germination (Fig. 3e,f;  
178 Extended Data Fig. 4f,g). This is consistent with reports that seeds and pollen accumulate  
179 storage molecules including mRNAs and proteins to allow rapid development at the onset of  
180 germination and likely explains the observed uncoupling of transcription and translation in these  
181 durable plant tissues<sup>29</sup>. Fluctuating PTRs of genes between tissues indicate tissue-specific  
182 regulation on either transcript or protein level. Conversely, genes with stable PTRs, are likely  
183 under similar regulation in different tissues and the extensive transcriptomic resources available  
184 for Arabidopsis may therefore be used to estimate relative protein abundances (Extended Data  
185 Fig. 5a,b). Similarly, stable ratios between p-site abundance and the corresponding protein  
186 levels, indicates that, under steady-state conditions, the majority of phosphorylation abundance  
187 changes between tissues can be attributed to fluctuations of the underlying protein abundance  
188 rather than phosphorylation stoichiometry (Extended Data Fig. 5c,d).

### 189 ***Co-expression of paralogs and complexes***

190 Based on the ‘guilt by association’ idea, gene co-expression analysis is widely used to ascribe  
191 common functionality between genes and can be performed on transcript or protein level. We  
192 observed that co-expressed gene pairs also have high STRING<sup>30</sup> scores, indicative of physical  
193 or functional interactions (Extended Data Fig. 6a). To illustrate this point, we focused on co-  
194 expression analyses of gene paralogs and interacting proteins. Arabidopsis, like most plants,  
195 has undergone genome duplications and retains a considerable number of highly conserved  
196 paralogs in the genome<sup>31</sup>. Compared to randomly selected gene pairs, duplicated genes show  
197 a clear shift towards positive expression correlations (both transcript and protein). This indicator  
198 for redundant gene function is supported by the finding that knock-out mutants of the more  
199 abundant paralog are more likely to display a measureable plant phenotype<sup>32</sup> (Extended Data

200 Fig. 6b-d; Supplementary Data 6). Such comparative expression analyses can be useful to  
201 prioritize knock-out combinations for phenotype analyses of functionally redundant genes.

202 Analyzing proteins that engage in physical interactions recorded in AtPIN<sup>33</sup> for co-expression  
203 across tissues suggests that ~26% of AtPIN pairs may be stable rather than transient complex  
204 partners (online methods; Extended Data Fig. 6e,f). As expected, protein-based correlations  
205 were consistently higher than transcript correlations. Because co-expression analyses tend to  
206 generate a large number of interaction candidates, we sought to prioritize these using data from  
207 size-exclusion chromatography-mass spectrometry experiments (SEC-MS) as an independent  
208 experimental approach<sup>34</sup> (Extended Data Fig. 7a-c; Supplementary Data 7,8). Indeed, we found  
209 that co-detection in SEC-MS, in addition to co-expression in the tissue atlas, substantially  
210 reduced the list of candidates, illustrated here by the detection of the coatomer complex in the  
211 intersection of the SEC-MS and tissue atlas data (Fig. 4a,b). The identification of known protein  
212 complexes was consistently improved by using this approach, which combines information from  
213 SEC and the tissue atlas datasets (Extended Data Fig. 7d, Supplementary Data 9, see online  
214 methods).

215 Interestingly, in seed tissues, the  $\zeta$ -subunit of the coatomer complex was almost exclusively  
216 provided by the  $\zeta$ -1 paralog, while this was almost absent in all other tissues (Extended Data  
217 Fig. 7e). Subunit abundance comparisons also provided information about complex  
218 stoichiometry and similar results were obtained for stable complexes when using the SEC-MS  
219 or tissue atlas dataset (Fig. 4c, Extended Data Fig. 7f,g). We, therefore, propose that our tissue  
220 atlas resource can provide an initial approximation of the relative subunit frequency of known  
221 complexes with unresolved stoichiometry. This could be particularly useful for membrane- or cell  
222 wall-associated complexes, which are difficult to study biochemically.

### 223 ***The Arabidopsis phosphoproteome***

224 The number of kinases ( $642 \pm 55$ ) and phosphatases ( $119 \pm 6$ ) as well as the ratios of individual  
225 families were comparable across most tissues. Pollen and egg cell-like callus, however, stood  
226 out implying extensive signaling activity in these tissues (Extended Data Figure 8a-c). In  
227 contrast to the wealth of available phosphoproteomic data to date, information on kinase-  
228 substrate relationships, critical for understanding signaling cascades or pathway activities, is still  
229 sparse. Because these relationships are difficult to discover experimentally, scientists often  
230 initially take a computational approach. We used the motif-X algorithm<sup>35</sup> to identify 266  
231 phosphorylation motifs that grouped into 'proline-directed', 'acidic', 'basic' or 'other' motif classes  
232<sup>36</sup> (Extended Data Figure 8d-f; Supplementary Table 2, Supplementary Data 10). Together with

233 information about the co-occurrence of kinases and p-sites in tissues, as well as external  
234 information like co-localization or interaction, we anticipate that this dataset can help untangle  
235 kinase-substrate and kinase-p-site relationships in the future.

236 Overall, the number of p-sites per protein showed vast variations. For example, members of the  
237 LEA protein family<sup>37</sup> are phosphorylated at almost every serine, threonine or tyrosine residue in  
238 their sequences (Fig. 5a; Extended Data Fig. 8g,h). Phosphorylation of these unstructured  
239 proteins involved in seed maturation and desiccation may be a mechanism to regulate their  
240 conformational state or phase transitions<sup>38</sup>. Conversely, other proteins showed p-site clusters in  
241 regulatory domains, including the juxtamembrane domain of receptor-like kinases<sup>39</sup> (Extended  
242 Data Figure 8i), implying a role in recruiting interaction partners akin to human receptor tyrosine  
243 kinases.

244 While the mere detection of a phosphorylation event does not directly imply a functional  
245 consequence, it provides important starting points<sup>40</sup>. For example, the abscisic acid (ABA)  
246 receptor RCAR10, involved in the ABA signaling cascade, was found to be phosphorylated at  
247 four sites. We generated phosphomimic mutants (S113D, S32D) that displayed reduced ABA  
248 response compared to the wild type receptor (Fig. 5b). While this might be linked to an effect on  
249 ABA binding or PP2C interaction for pS113 which is part of the interaction surface for protein  
250 phosphatase 2 (PP2Cs) co-receptors, it is more likely due to altered interactions with other  
251 regulatory proteins for pS32, which is localized at the receptor periphery<sup>41</sup> (Extended Data Fig.  
252 9a,b). Interestingly, both RCAR10 phosphomimic variants altered the ABA response of  
253 RCAR10-PP2C co-receptor combinations, suggesting changes in the interaction profile and  
254 phosphorylation-based fine-tuning of ABA signaling during development and stress response  
255 (Extended Data Fig. 9c,d).

256 As a second example for functional consequences of protein phosphorylation, we studied QKY,  
257 a protein localized to plasmodesmata and involved in floral and silique morphogenesis<sup>42</sup>. Since  
258 one of its p-sites (S262) was detected in all assayed tissues and further p-sites were found  
259 between the first and second C2 domains in other MCTP family members, we speculated about  
260 a possible effect of pS262 on QKY function (Extended Data Fig. 9e,f). To test this hypothesis,  
261 we generated plant lines expressing phosphomimic and phosphomutant QKY transgenes in the  
262 strong *qky-9* mutant background<sup>43</sup>. The data show that phosphomimic but not phosphomutant  
263 protein constructs rescued both flower and silique mutant phenotypes, suggesting that  
264 phosphorylation of S262 is required for normal QKY function (Fig. 5c-f, Extended Data Fig. 9g-  
265 j).



266 Taken together, we have generated the most comprehensive, albeit still incomplete, draft of the  
267 Arabidopsis (phospho)proteome to date and highlighted some of the many uses that can be  
268 envisioned for this resource. Yet, much remains to be accomplished including a more  
269 systematic coverage of protein sequence variants or post-translational modifications. The tens  
270 of thousands of newly discovered phosphorylation sites that await functional characterization  
271 present a particular future challenge. The examples we provide demonstrate that investigating  
272 different levels of omics data can lead to new insights into biological processes. We therefore  
273 anticipate that this resource along with the provided online computational tools will enable the  
274 Arabidopsis research community to perform many further types of systems-level analyses not  
275 covered here. We also expect that the study will more broadly impact plant research as the work  
276 demonstrates that mass spectrometry-based quantitative protein assays are a veritable way to  
277 overcome the disabling lack of antibodies for plant research.  
278

279 **References**

280 1 Kramer, U. Planting molecular functions in an ecological context with *Arabidopsis thaliana*. *Elife*  
281 **4**, doi:10.7554/eLife.06100 (2015).

282 2 Peng, J. *et al.* 'Green revolution' genes encode mutant gibberellin response modulators. *Nature*  
283 **400**, 256-261, doi:10.1038/22307 (1999).

284 3 Arabidopsis Genome, I. Analysis of the genome sequence of the flowering plant *Arabidopsis*  
285 *thaliana*. *Nature* **408**, 796-815, doi:10.1038/35048692 (2000).

286 4 Kawakatsu, T. *et al.* Epigenomic Diversity in a Global Collection of *Arabidopsis thaliana*  
287 Accessions. *Cell* **166**, 492-505, doi:10.1016/j.cell.2016.06.044 (2016).

288 5 Cheng, C. Y. *et al.* Araport11: a complete reannotation of the *Arabidopsis thaliana* reference  
289 genome. *Plant J* **89**, 789-804, doi:10.1111/tpj.13415 (2017).

290 6 The UniProt, C. UniProt: the universal protein knowledgebase. *Nucleic Acids Res* **45**, D158-D169,  
291 doi:10.1093/nar/gkw1099 (2017).

292 7 Baerenfaller, K. *et al.* Genome-scale proteomics reveals *Arabidopsis thaliana* gene models and  
293 proteome dynamics. *Science* **320**, 938-941, doi:10.1126/science.1157956 (2008).

294 8 van Wijk, K. J., Friso, G., Walther, D. & Schulze, W. X. Meta-Analysis of *Arabidopsis thaliana*  
295 Phospho-Proteomics Data Reveals Compartmentalization of Phosphorylation Motifs. *Plant Cell*  
296 **26**, 2367-2389, doi:10.1105/tpc.114.125815 (2014).

297 9 Durek, P. *et al.* PhosPhAt: the *Arabidopsis thaliana* phosphorylation site database. An update.  
298 *Nucleic Acids Res* **38**, D828-834, doi:10.1093/nar/gkp810 (2010).

299 10 Sharma, K. *et al.* Ultradeep human phosphoproteome reveals a distinct regulatory nature of Tyr  
300 and Ser/Thr-based signaling. *Cell Rep* **8**, 1583-1594, doi:10.1016/j.celrep.2014.07.036 (2014).

301 11 Schmidt, T. *et al.* ProteomicsDB. *Nucleic Acids Res* **46**, D1271-D1281, doi:10.1093/nar/gkx1029  
302 (2018).

303 12 Gessulat, S. *et al.* ProSIT: proteome-wide prediction of peptide tandem mass spectra by deep  
304 learning. *Nat Methods* **16**, 509-518, doi:10.1038/s41592-019-0426-7 (2019).

305 13 Bienvenut, W. V. *et al.* Comparative large scale characterization of plant versus mammal  
306 proteins reveals similar and idiosyncratic N-alpha-acetylation features. *Mol Cell Proteomics* **11**,  
307 M111 015131, doi:10.1074/mcp.M111.015131 (2012).

308 14 Hazarika, R. R. *et al.* ARA-PEPs: a repository of putative sORF-encoded peptides in *Arabidopsis*  
309 *thaliana*. *BMC Bioinformatics* **18**, 37, doi:10.1186/s12859-016-1458-y (2017).

310 15 Wilhelm, M. *et al.* Mass-spectrometry-based draft of the human proteome. *Nature* **509**, 582-  
311 587, doi:10.1038/nature13319 (2014).

312 16 Zheng, Y. *et al.* iTAK: A Program for Genome-wide Prediction and Classification of Plant  
313 Transcription Factors, Transcriptional Regulators, and Protein Kinases. *Mol Plant* **9**, 1667-1670,  
314 doi:10.1016/j.molp.2016.09.014 (2016).

315 17 Yang, M. *et al.* A comprehensive analysis of protein phosphatases in rice and *Arabidopsis*. *Plant*  
316 *Systematics and Evolution* **289**, 111-126, doi:10.1007/s00606-010-0336-8 (2010).

317 18 Litt, A. & Kramer, E. M. The ABC model and the diversification of floral organ identity. *Semin Cell*  
318 *Dev Biol* **21**, 129-137, doi:10.1016/j.semcd.2009.11.019 (2010).

319 19 Bar-On, Y. M. & Milo, R. The global mass and average rate of rubisco. *Proc Natl Acad Sci U S A*  
320 **116**, 4738-4743, doi:10.1073/pnas.1816654116 (2019).

321 20 Gupta, R. *et al.* Time to dig deep into the plant proteome: a hunt for low-abundance proteins.  
322 *Front Plant Sci* **6**, 22, doi:10.3389/fpls.2015.00022 (2015).

323 21 Galvan-Ampudia, C. S. & Offringa, R. Plant evolution: AGC kinases tell the auxin tale. *Trends*  
324 *Plant Sci* **12**, 541-547, doi:10.1016/j.tplants.2007.10.004 (2007).

325 22 Zhang, Y., He, J. & McCormick, S. Two Arabidopsis AGC kinases are critical for the polarized  
326 growth of pollen tubes. *Plant J* **58**, 474-484, doi:10.1111/j.1365-313X.2009.03792.x (2009).

327 23 Eraslan, B. *et al.* Quantification and discovery of sequence determinants of protein-per-mRNA  
328 amount in 29 human tissues. *Mol Syst Biol* **15**, e8513, doi:10.15252/msb.20188513 (2019).

329 24 Liu, Y., Beyer, A. & Aebersold, R. On the Dependency of Cellular Protein Levels on mRNA  
330 Abundance. *Cell* **165**, 535-550, doi:10.1016/j.cell.2016.03.014 (2016).

331 25 Hanson, G. & Collier, J. Codon optimality, bias and usage in translation and mRNA decay. *Nat Rev*  
332 *Mol Cell Biol* **19**, 20-30, doi:10.1038/nrm.2017.91 (2018).

333 26 Schwanhauser, B. *et al.* Global quantification of mammalian gene expression control. *Nature*  
334 **473**, 337-342, doi:10.1038/nature10098 (2011).

335 27 Santner, A. & Estelle, M. The ubiquitin-proteasome system regulates plant hormone signaling.  
336 *Plant J* **61**, 1029-1040, doi:10.1111/j.1365-313X.2010.04112.x (2010).

337 28 Luo, J., Zhou, J. J. & Zhang, J. Z. Aux/IAA Gene Family in Plants: Molecular Structure, Regulation,  
338 and Function. *Int J Mol Sci* **19**, doi:10.3390/ijms19010259 (2018).

339 29 Bai, B. *et al.* Seed stored mRNAs that are specifically associated to monosome are translationally  
340 regulated during germination. *Plant Physiol*, doi:10.1104/pp.19.00644 (2019).

341 30 Szklarczyk, D. *et al.* The STRING database in 2017: quality-controlled protein-protein association  
342 networks, made broadly accessible. *Nucleic Acids Res* **45**, D362-D368, doi:10.1093/nar/gkw937  
343 (2017).

344 31 Wang, Y., Tan, X. & Paterson, A. H. Different patterns of gene structure divergence following  
345 gene duplication in Arabidopsis. *BMC Genomics* **14**, 652, doi:10.1186/1471-2164-14-652 (2013).

346 32 Lloyd, J. & Meinke, D. A comprehensive dataset of genes with a loss-of-function mutant  
347 phenotype in Arabidopsis. *Plant Physiol* **158**, 1115-1129, doi:10.1104/pp.111.192393 (2012).

348 33 Brandao, M. M., Dantas, L. L. & Silva-Filho, M. C. AtPIN: Arabidopsis thaliana protein interaction  
349 network. *BMC Bioinformatics* **10**, 454, doi:10.1186/1471-2105-10-454 (2009).

350 34 Kristensen, A. R., Gsponer, J. & Foster, L. J. A high-throughput approach for measuring temporal  
351 changes in the interactome. *Nat Methods* **9**, 907-909, doi:10.1038/nmeth.2131 (2012).

352 35 Schwartz, D & Gygi, SP. An iterative statistical approach to the identification of protein  
353 phosphorylation motifs from large-scale data sets. *Nat Biotechnology* **23**1391-1398,  
354 doi:10.1038/nbt1146 (2005).

355 36 Villen, J., Beausoleil, S. A., Gerber, S. A. & Gygi, S. P. Large-scale phosphorylation analysis of  
356 mouse liver. *Proc Natl Acad Sci U S A* **104**, 1488-1493, doi:10.1073/pnas.0609836104 (2007).

357 37 Battaglia, M., Olvera-Carrillo, Y., Garcarrubio, A., Campos, F. & Covarrubias, A. A. The enigmatic  
358 LEA proteins and other hydrophilins. *Plant Physiol* **148**, 6-24, doi:10.1104/pp.108.120725 (2008).

359 38 Bah, A. *et al.* Folding of an intrinsically disordered protein by phosphorylation as a regulatory  
360 switch. *Nature* **519**, 106-109, doi:10.1038/nature13999 (2015).

361 39 Mitra, S. K. *et al.* An autophosphorylation site database for leucine-rich repeat receptor-like  
362 kinases in Arabidopsis thaliana. *Plant J* **82**, 1042-1060, doi:10.1111/tpj.12863 (2015).

363 40 Landry, C. R., Levy, E. D. & Michnick, S. W. Weak functional constraints on phosphoproteomes.  
364 *Trends Genet* **25**, 193-197, doi:10.1016/j.tig.2009.03.003 (2009).

365 41 Hauser, F., Li, Z., Waadt, R. & Schroeder, J. I. SnapShot: Abscisic Acid Signaling. *Cell* **171**, 1708-  
366 1708 e1700, doi:10.1016/j.cell.2017.11.045 (2017).

367 42 Vaddepalli, P. *et al.* The C2-domain protein QUIRKY and the receptor-like kinase STRUBBELIG  
368 localize to plasmodesmata and mediate tissue morphogenesis in Arabidopsis thaliana.  
369 *Development* **141**, 4139-4148, doi:10.1242/dev.113878 (2014).

370 43 Fulton, L. *et al.* DETORQUEO, QUIRKY, and ZERZAUST represent novel components involved in  
371 organ development mediated by the receptor-like kinase STRUBBELIG in Arabidopsis thaliana.  
372 *PLoS Genet* **5**, e1000355, doi:10.1371/journal.pgen.1000355 (2009).



374 **Figure legends**

375 **Figure 1 | Tissue map and multi-omics dataset.** a, Schematic representation of tissue  
376 samples analysed in this study and coloured according to morphology group: Flower (light grey),  
377 seed (dark brown), pollen (yellow), stem (dark green), leaf (light green), root (dark grey), fruit  
378 (light brown), callus (magenta), cell culture (blue). b, Number of identifications at the protein,  
379 transcript and phosphorylation site (p-site) level for all tissues (n = 1 measurements per tissue).  
380 A dashed line indicates the number of core proteins, transcripts or p-sites detected in all tissues.  
381 Tissue-enhanced proteins or transcripts are marked in darker colour. P-sites with high  
382 confidence amino acid localization (class I, >0.75 localization probability) are shown in pink,  
383 ambiguous site localizations in purple. The number of p-sites exclusively detected in one tissue  
384 is shown as circles. c, Total number and overlap of identified gene loci in the transcriptome,  
385 proteome and phosphoproteome datasets compared to Araport11 (left panel) and total number  
386 of identified p-sites and proportion of class I sites (right panel).

387 **Figure 2 | Data exploration in ATHENA and ProteomicsDB.** a, Schematic representation of  
388 data analysis options in the web tool ATHENA (Arabidopsis THaliana ExpressioN Atlas) and  
389 ProteomicsDB. b, Mirror plot showing near identical observed and predicted tandem mass  
390 spectra (n = 1 acquired spectra) for a peptide from the 'uncertain' protein AT4G13955, thus  
391 validating its existence as a protein. SA denotes the normalized spectral contrast angle, a  
392 measure for spectrum similarity. c, Upper panel: summed absolute protein expression of AGC1  
393 and AGC3 subfamilies of AGCVIII kinases. Lower panel: relative protein expression profiles of  
394 D6PK family members and the closely related kinases AGC1.5, AGC1.6 and AGC1.7. Arrow  
395 heads indicate embryo and pollen tissue with high expression of D6PKL3 or AGC1.5 and  
396 AGC1.7, respectively. d-e, Representative images of GUS-stained flowers expressing *AGC1.6*  
397 (n = 20 independent transgenic lines) and *AGC1.7* (n = 12 independent transgenic lines)  
398 promotor-GUS fusions. Arrow-heads indicate anthers containing pollen grains. Scale bars 1  
399 mm. f-i, Representative images of embryo phenotypes (at heart stage or age matched  
400 equivalent) and their respective frequency for wild type (WT), *d6pk13* single, *d6pk012* triple  
401 (*d6pk d6pk1 d6pk2*) and *d6pk0123* (*d6pk d6pk1 d6pk2 d6pk3*) quadruple knock-out mutants.  
402 Scale bars 20  $\mu$ m.

403 **Figure 3 | Protein and mRNA expression.** a, Scatter plot of protein versus transcript  
404 abundance (median across 30 tissues). Arrows mark examples for genes with high protein to  
405 transcript ratio (PTR, *rbcL*, *petA*) or low PTR (*IAA8*, *IAA13*). Pearson correlation (*R*). b, Relative  
406 contribution of molecular features (averaged across tissues) able to predict protein abundance.  
407 UTR, untranslated region, Dn/Ds, ratio of non-synonymous to synonymous nucleotide  
408 substitutions. c, Schematic representation of the steps where modulation of PTRs may occur.  
409 For example, the higher the transcription rate the lower the PTR. d, PTR distribution of genes  
410 for selected tissues. Genes with high and low PTRs are defined as being outside two standard  
411 deviations of the median PTR distribution. e, Analysis of the proportion of genes with high or low

412 PTRs that are at least 4-fold differently abundant on transcript and/or protein level in seed  
413 compared to all other tissues (depicted as arrows). The percentage of genes below the 4-fold  
414 criterion are placed at the origin of the plot. n denotes the number of genes with high or low  
415 PTRs in seed as defined in panel d. f, Relative protein expression changes of proteins with high  
416 or low PTRs (from panel e) in seeds incubated for 8h, 16h and 24h with 100  $\mu$ M cycloheximide  
417 (translation block), MG132 (proteasome block) or DMSO (control).

418 **Figure 4 | Protein complex characterization by protein co-expression and SEC-MS.** a,  
419 Upper panel: 221 proteins that form a module in the tissue atlas based on their co-expression  
420 across all tissues. Lower panel: co-elution of 57 proteins in a size-exclusion chromatography  
421 (SEC)-mass spectrometry experiment using flower tissue. b, Overlap of proteins (n=14)  
422 between the groups of co-expressed and co-eluting proteins in a. Ten of the proteins in the  
423 intersection are subunits of the coatomer complex. c, Tissue-resolved absolute abundance (top  
424 panel) and relative proportions of coatomer complex subunits based on the tissue atlas protein  
425 expression data (lower panel) showing heterogeneous expression but a fairly homogeneous  
426 composition of the complex across tissues. Paralogs of the  $\alpha$ ,  $\beta$ ,  $\beta'$ ,  $\epsilon$  and  $\zeta$  coatomer subunits  
427 were combined for the analysis. Tissue groups are coloured as in Figure 1.

428 **Figure 5 | Ascribing function to protein phosphorylation.** a, Scatter plot of the proportion of  
429 potential phosphorylation acceptor sites in a protein sequence (limited to S, T and Y) versus the  
430 proportion of STY residues found to be phosphorylated in this study. While most proteins  
431 including RCAR10 and QKY show only a small proportion of phosphorylated residues, the LEA  
432 proteins are phosphorylated at almost every possible residue. b, Abscisic acid (ABA) response  
433 (average  $\pm$  SD; n = 3) of ABA treated protoplast cells transformed with wild type or  
434 phosphomimic variants of RCAR10 (S32D and S113D) suggesting that S32 and S113  
435 phosphorylation are functionally involved in RCAR10 activity. c-f, Representative images of  
436 flowers and siliques of wild type (WT), *qky-9* mutant and *qky-9* expressing phospho-dead  
437 QKY<sub>S262A</sub> or phosphomimic QKY<sub>S262E</sub> constructs showing that QKY<sub>S262E</sub> but not QKY<sub>S262A</sub>  
438 rescues the *qky-9* phenotype. Scale bars: flower 1 mm, silique 0.5 cm.

439

## 440 **Methods**

### 441 ***Sample preparation***

442 ***Inflorescence and seed samples:*** *Arabidopsis thaliana* wild type Columbia-0 (Col-0) plants  
443 were grown under continuous white light conditions at 22°C. Samples for flower parts and  
444 siliques were harvested from mature plants. Stage 15 flowers<sup>46</sup> were dissected into petal,  
445 sepal, stamen and carpel. Fully grown green siliques were separated into septum, valves and  
446 green seeds (stage 10). Surface-sterilized mature dry seeds were stored for two days at 4°C  
447 and subsequently imbibed for 24 h or kept dry. For pollen collection, plants were grown on soil  
448 under a long photoperiod (16 h of light, 21°C, 65% humidity). Mature pollen was bulk-harvested  
449 from open flowers at developmental stage 13<sup>46</sup>. A vacuum cleaner was modified with three  
450 subsequent nylon meshes (80 micron, 35 micron, 10 micron mesh) for large scale pollen  
451 isolation as described<sup>47</sup>. Pollen was collected in a 1.5 ml reaction tube, snap-frozen in liquid  
452 nitrogen and stored at -80°C until further use.

453 ***Cell culture and callus samples:*** Cell culture samples (root cells, Col-0) were grown in  
454 medium composed of 4.3 g/l Murashige and Skoog basal medium (MS), 30 g/l sucrose and 0.33  
455 mg/ml KH<sub>2</sub>PO<sub>4</sub>, supplemented with 2,4-D (final concentration 1 mg/l; pH adjusted to 5.8 with  
456 KOH) at 22°C under continuous light and harvested either three or ten days after sub-culturing.  
457 To generate callus inducing medium (CIM) callus, root explants were harvested from two  
458 weeks-old seedlings (Col-0) grown in sterile culture on MS plates. 5 to 10 mm long root  
459 segments were cultured on CIM medium composed of 1x Gamborg's B-5 salts, 20 g/l glucose,  
460 0.5 g/l MES, 1x Gamborg's vitamin solution and 1% Phytoagar supplemented with 2,4-D (500  
461 µg/l) and kinetin (50 µg/l). CIM calli appeared after 7 to 10 days and were propagated in two  
462 weeks-subculture intervals on CIM medium. To generate the callus line with an egg cell-like  
463 expression profile, the coding sequence of RKD2 (AT1G74480) was amplified from pistil cDNA  
464 using the primer pair RKD2fw and RKD2rev (Supplementary Data 11). Pistils from flowers at  
465 developmental stage 12<sup>47</sup> were harvested to purify mRNA and generate cDNA as described<sup>48</sup>.  
466 The PCR fragment was cloned into pENTR/D-TOPO (Invitrogen, Carlsbad, USA) and  
467 subsequently transferred into the GATEWAY-compatible destination vector pH7FWG2.0<sup>49</sup> with  
468 LR clonase. The resulting expression vector 35Sp:RKD2-GFP was used for floral dip  
469 transformation of *Arabidopsis*<sup>50</sup>. Seeds of transformed plants were surface-sterilized and grown  
470 on ½ MS medium with 2% (w/v) sucrose, 1% Phytoagar, and Hygromycin (30 µg/ml). RKD2-  
471 induced calli had formed after 20 to 30 days and were propagated in two weeks-subculture

472 intervals on ½ MS, 2% (w/v) sucrose, 1% Phytoagar, Hygromycin (30 µg/ml). Calli were  
473 collected with a sterile scalpel blade and immediately frozen in liquid nitrogen.

474 **Leaf and root samples:** Arabidopsis plants (Col-0) were grown under continuous light  
475 conditions at 22°C. Senescent rosette leaves were collected from 35 days-old plants. Samples  
476 for stem, first node, second internode and first cauline leaf were collected from 30 days-old  
477 plants. Rosette leaf sections (Leaf7: distal; proximal; petiole) were harvested from 22 days-old  
478 plants before bolting. Seedlings were grown on ½ MS plates under continuous light for  
479 seven days and separated into cotyledons, hypocotyl, root tip, root maturation zone or seed  
480 apical meristem including cotyledons and first leaves. Whole roots were harvested from 22  
481 days-old plants grown under continuous light on ½ MS plates.

482 Classification of growth stage and plant section was done as described <sup>44,51-53</sup>. Harvested  
483 material from at least three individual plants was combined for each sample, frozen in liquid  
484 nitrogen and stored at -80°C until further use.

#### 485 **Protein lysis and digest**

486 Frozen plant material was homogenized with a tissue lyzer (Qiagen, Hilden, Germany) or with  
487 mortar and pestle in liquid nitrogen. Proteins were precipitated over night with 10%  
488 trichloroacetic acid in acetone at -20° C and subsequently washed two times with ice-cold  
489 acetone. Dry samples were incubated with urea digestion buffer (8 M urea, 50 mM Tris-HCl pH  
490 7.5, 1 mM DTT, cOmplete™ EDTA-free protease inhibitor cocktail (PIC) [Roche, Basel,  
491 Switzerland], Phosphatase inhibitor [PI-III; in-house, composition resembling Phosphatase  
492 inhibitor cocktail 1,2 and 3 from Sigma-Aldrich, St. Louis, USA]) for 1 h. Protein concentration  
493 was determined with a Bradford assay <sup>54</sup>. 1 mg of protein was reduced (10 mM DTT, 1h, room  
494 temperature), alkylated (55 mM chloroacetamide, 30min, room temperature) and subsequently  
495 diluted 1:8 with digestion buffer (50 mM Tris-HCl pH 8.0, 1 mM CaCl<sub>2</sub>). In-solution pre-digestion  
496 with trypsin (Roche, Basel, Switzerland) was performed for 4 hours at 37°C (1:100  
497 protease:protein ratio), followed by overnight digestion with trypsin (1:100 protease:protein  
498 ratio). Samples were acidified to pH 3 using trifluoroacetic acid (TFA) and centrifuged at  
499 14,000 g for 15 min at 4°C. The supernatant was desalted on 50 mg SepPAC SPE cartridges  
500 (Waters, Milford, USA). Peptides were eluted with 0.1 % TFA in 50% acetonitrile (ACN) and  
501 vacuum-dried in a Thermo Savant SPD SpeedVac (Thermo Fisher Scientific, Waltham, USA).

#### 502 **Peptide enrichment and off-line fractionation**



503 Fe<sup>3+</sup>-IMAC was performed as described previously with some adjustments<sup>55</sup>. Briefly, desalted  
504 peptide samples were re-suspended in ice-cold IMAC loading buffer (0.1% TFA, 40% ACN). For  
505 quality control, 1.5 nmol of a synthetic library of phosphopeptides and their corresponding non-  
506 phosphorylated counterpart sequence (B2 and F1)<sup>56</sup> were spiked into each sample prior to  
507 loading onto a Fe<sup>3+</sup>-IMAC column (Propac IMAC-10 4x50 mm, Thermo Fisher Scientific,  
508 Waltham, USA). The enrichment was performed with Buffer A (0.07% TFA, 30% ACN) as wash  
509 buffer and Buffer B (0.315% NH<sub>4</sub>OH) as elution buffer. Collected full proteome and  
510 phosphopeptide fractions were vacuum-dried and stored at -80°C until further use.

511 For the full proteome fraction, hydrophilic strong anion exchange chromatography (hSAX)  
512 peptide separation was performed as described previously<sup>15</sup>. Briefly, an equivalent of 300 µg  
513 protein digest was reconstituted in hSAX solvent A (5 mM Tris-HCl, pH 8.5) and separated  
514 using a Dionex Ultimate 3000 HPLC system (Dionex Cor., Idstein, Germany) equipped with an  
515 IonPac AG24 guard column (2x50 mm) and an IonPac AS24 strong anion exchange column (2x  
516 250 mm, Thermo Fisher Scientific, Waltham, USA). Fractions were collected in 96 well format  
517 and subsequently pooled to 24. Individual fractions were acidified with formic acid (FA),  
518 desalted on self-packed StageTips (five disks, Ø 1.5 mm C18 material, 3M Empore™, elution  
519 solvent 0.1% FA in 50% ACN) and dried down prior to LC-MS/MS analysis. Phosphopeptide  
520 fractions were separated into four fractions using a StageTip (five disks, Ø 1.5 mm C18  
521 material, 3M Empore™) based high pH reversed phase protocol as described previously<sup>57</sup>.  
522 Phosphopeptides were eluted with 2.5%, 7.5%, 12.5% and 50% ACN in 25 mM NH<sub>4</sub>FA pH  
523 10. The flow through and 50% ACN fraction were combined and all fractions were dried down  
524 prior to LC-MS/MS analysis.

525 For the cycloheximide and MG132 chase experiments, 300 µg peptides for each sample were  
526 reconstituted in high pH reversed phase loading buffer (2.5 mM NH<sub>4</sub>HCO<sub>3</sub>, pH 8) and  
527 fractionated using a Dionex Ultimate 3000 HPLC system (Dionex Corp., Idstein, Germany) and  
528 a Waters XBridge column (BEH130 C18, 3.5 µm, 2.1x150mm; Waters, Milford, USA). Peptides  
529 were separated by a linear gradient from 4% Buffer D to 32% D in 45 min, followed by a linear  
530 gradient from 32% D to 80% D in 6 min. The proportion of Buffer A was kept at 10% during  
531 fractionation (Buffer A: 25 mM NH<sub>4</sub>HCO<sub>3</sub>, pH 8; Buffer C: 100% ACN; Buffer D: 100% ultrapure  
532 water). Fractions were collected in 96 well format, subsequently pooled to 48, acidified and  
533 dried in a SpeedVac.

534 ***Seed treatment with cycloheximide and MG132***

535 Aliquots of surface-sterilized mature dry seeds ((10 mg, Col-0) were stored for two days at 4°C  
536 in the dark and subsequently imbibed with 2 ml liquid ½ MS at 22°C under constant light. After 4  
537 h incubation, cycloheximide (CHX) or MG132 (*N*-(benzyloxycarbonyl)-Leu-Leu-Leu-al) was  
538 added to a concentration of 100 µM. Since both CHX and MG132 were dissolved at the same  
539 stock concentration in 100% dimethylsulfoxide (DMSO), the respective volume of 100% DMSO  
540 was added to the control samples. As a baseline sample, one seed aliquot was dried and  
541 immediately frozen in liquid nitrogen after the 4 h incubation in ½ MS medium. Seeds for CHX,  
542 MG132 and DMSO control were removed after 8 h, 16 h and 24 h treatment, dried and frozen in  
543 liquid nitrogen. Germination of treated seeds was visually checked after 4 days of incubation.  
544 Both compounds CHX and MG132 were active and led to complete or partial inhibition of seed  
545 germination as compared to a DMSO treated control sample (Extended Data Fig. 4i).

546 Protein extraction and digest was performed as described above. Peptide quantification prior to  
547 high pH reversed phase fractionation was done using the Pierce™ BCA protein assay kit  
548 (Thermo Fisher Scientific, Waltham, USA) <sup>58</sup>.

#### 549 ***Size exclusion chromatography (SEC)***

550 Homogenized flower (stage 15), leaf (rosette leaf 7) and root (whole root) samples were lysed in  
551 ice-cold 50 mM Tris-HCl pH 7.4, 100 mM NaCl, 10% glycerin, PIC, PI-III and 0.1% Triton-X100.  
552 After filtering (Ø 0.2µm), 0.25 ml lysate containing 1 mg of protein was injected on a Superose 6  
553 10/30 GL column (GE Healthcare, Chicago, USA) and separated at a flow rate of 250 µl/min on  
554 an Äkta pure 25 (GE Healthcare, Chicago, USA). Molecular weight calibration of the column  
555 was performed with the high molecular weight gel filtration calibration kit (GE Healthcare,  
556 Chicago, USA). After the void volume, 80 fractions of 125 µl each were collected, vacuum dried  
557 and re-solubilized in urea digestion buffer. In-solution digestion with trypsin and sample  
558 desalting on self-packed StageTips was performed as described above. For quality control,  
559 PROCAL peptide standard <sup>59</sup> was spiked into each SEC fraction prior to LC-MS/MS analysis.

#### 560 ***LC-MS/MS analysis***

561 Nanoflow LC-MS/MS was performed by coupling a Dionex 3000 (Thermo Fisher Scientific,  
562 Waltham, USA) to a QExactive Orbitrap HF (Thermo Fisher Scientific, Waltham, USA). Samples  
563 for the proteome and phosphoproteome analysis were re-suspended in loading buffer  
564 containing 0.1% formic acid (FA) or 50 mM citrate and 1% FA, respectively. Peptide loading and  
565 washing were done on a trap column (100 µm i.d. x 2 cm, packed in-house with Reprosil-Pur  
566 C18-GOLD, 5 µm resin, Dr. Maisch, Ammerbuch, Germany) at a flow rate of 5 µl/min in 100%

567 loading buffer (0.1% FA) for 10 min. Peptide separation was performed on an analytical column  
568 (75  $\mu\text{m}$  i.d. x 40 cm packed in-house with Reprosil-Pur C18, 3  $\mu\text{m}$  resin, Dr. Maisch,  
569 Ammerbuch, Germany) at a flow rate of 300 nl/min using a 110 min gradient from 4% to 32%  
570 solvent B (solvent A: 0.1% FA, 5% DMSO in HPLC grade water; solvent B: 0.1% FA, 5% DMSO  
571 in acetonitrile) for the tissue map full proteome analysis and a two-step 110 min gradient from  
572 2% to 27% solvent B for the phosphoproteome analysis<sup>60</sup>. Peptides were ionized using a spray  
573 voltage of 2.2 kV and a capillary temperature of 275°C. The instrument was operated in data-  
574 dependent mode, automatically switching between MS and MS2 scans. For the full proteome  
575 samples of the tissue atlas experiment, full scan MS spectra ( $m/z$  360 – 1300) were acquired  
576 with a maximum injection time of 10 ms at 60,000 resolution and an automatic gain control  
577 (AGC) target value of 3e6 charges. For the top 12 precursor ions, high resolution MS2 spectra  
578 were acquired in the orbitrap with a maximum injection time of 50 ms at 15,000 resolution  
579 (isolation window 1.7  $m/z$ ), an AGC target value of 2e5 and normalized collision energy of 25%.  
580 The underfill ratio was set to 1% with a dynamic exclusion of 30 s. Only precursors with charge  
581 states between 2 and 6 were selected for fragmentation. For the phosphoproteome analysis, the  
582 MS2 spectra were acquired with a resolution of 30,000 (isolation window 1.7  $m/z$ ) and a  
583 maximum injection time of 120 ms. Dynamic exclusion was set to 35 s.

584 SEC samples were measured using a 60 min 4% to 32% gradient. MS2 spectra were generated  
585 for the top 20 precursors, with a maximum injection time of 50 ms at 30,000 resolution (isolation  
586 window 1.7  $m/z$ ), a normalized collision energy of 25% and a dynamic exclusion of 20 s.

587 The samples for cycloheximide and MG132 treated seed samples were analyzed by a micro-  
588 flow LC system coupled online to an Orbitrap Fusion Lumos mass spectrometer (Thermo Fisher  
589 Scientific, Waltham, USA)) as described previously<sup>61</sup>. The micro LC system was built by  
590 combining a modified Vanquish pump with the auto-sampler of the Dionex UltiMate 3000  
591 RSLCnano System. The sample was directly loaded onto a Thermo Fisher Scientific Acclaim  
592 PepMap 100 C18 LC column (2  $\mu\text{m}$  particle size, 1 mm ID x 150 mm), the flow rate was 50  
593  $\mu\text{l}/\text{min}$  and column temperature was maintained at 55 °C. A 15 min linear gradient of 7%-32%  
594 solvent B (solvent A: 0.1% FA, 3% DMSO in HPLC grade water; solvent B: 0.1% FA, 3% DMSO  
595 in acetonitrile) was used to separate all the samples, followed by 1 min 95% solvent B washing  
596 and 1 min 0.5% solvent B equilibrium time at a flow rate of 100  $\mu\text{l}/\text{min}$ . The Orbitrap Fusion  
597 Lumos mass spectrometer was operated with the Ion Max API Source installed with a HESI-II  
598 probe (50  $\mu\text{m}$  ID). The detailed acquisition parameters are: Positive polarity; spray voltage 3.5  
599 kV, funnel RF lens value at 40, capillary temperature of 325 °C, auxiliary gas heater

600 temperature of 300 °C. The flow rates for sheath gas, aux gas and sweep gas were set to 32, 5,  
601 and 0, respectively. Full scan MS spectra (m/z 360 – 1300) were acquired in the orbitrap with a  
602 maximum injection time of 10 ms at 120,000 and an AGC target of 4E5. MS2 spectra were  
603 acquired in the linear ion trap (rapid scan mode) after collision-induced dissociation (CID)  
604 fragmentation with collision energy set at 35%, an AGC target of 1E4 and maximum IT of  
605 10 ms. The isolation window was set to 0.4 m/z and scans were recorded with a maximum duty  
606 cycle of 0.6 s and the option ‘inject ions for all parallelizable time’ enabled. Only precursors with  
607 charge states between 2 and 6 were selected for fragmentation and the lowest scan range of  
608 MS2 was fixed at 100 m/z. The intensity threshold was set to 5E3 and the dynamic exclusion to  
609 12 s.

### 610 ***Peptide and protein identification and quantification***

611 Raw data files were searched with MaxQuant software (v. 1.5.8.3) using standard settings  
612 unless otherwise described <sup>62</sup>. MS/MS spectra were searched against Araport11 <sup>5</sup> protein  
613 coding genes (Araport11\_genes.201606.pep.fasta; download 06/2016), with trypsin as protease  
614 and up to two allowed missed cleavages. Carbamidomethylation of cysteines was set as fixed  
615 modification and oxidation of methionines and N-terminal acetylation as variable modifications.  
616 The ‘match-between-runs’ function was enabled for corresponding fractions within one  
617 parameter set, where applicable.

618 For the tissue map analysis, full proteome and phosphoproteome samples were processed  
619 together as two separate parameter groups, with phosphorylation of serine, threonine or  
620 tyrosine defined as variable modification only for the phosphoproteome group. Here we also  
621 added the spike-in phosphopeptide library sequences <sup>56</sup> to the database search space.

622 For sORF identification two sORF databases (ATSO and ARA-PEP) were added to the search  
623 space in addition to Araport11. ARA-PEP is a previously described repository of putative sORF-  
624 encoded peptides in Arabidopsis <sup>14</sup>. ATSO (*Arabidopsis thaliana* sORFs) was generated by  
625 using sORFfinder <sup>63</sup> and our RNA-seq analysis data to identify putative new sORFs in non-  
626 coding intergenic regions (ATSO.non\_coding.pep.nr.cd-hit\_aS1\_aL0.3\_c1.out.nr.fasta). Three  
627 targets were used as input for sORFfinder. Sequences of intergenic and non-coding regions  
628 relative to the Araport11 annotation and sequences resulting from a Trinity <sup>64</sup> *de novo*  
629 transcriptome assembly which are non-overlapping with the Araport11 annotations. Afterwards,  
630 the sORF nucleotide sequences were translated to amino acid sequences. CD-HIT <sup>65</sup> was used  
631 with the parameters –aS 1 –aL 0.3 –c 1 to reduce sequence redundancy. .

632 SEC experiment raw files for flower, leaf and root were all searched together, with each SEC  
633 fraction designated as individual experiment and the 'match-between-runs' function enabled.

634 The seed experiment raw files were searched using standard settings as described above.

635 Peak list files generated by Baerenfaller et al. (2008) <sup>7</sup> were downloaded from Pride  
636 (PRD000044) and searched with the Mascot <sup>66</sup> search engine (version 2.4.1, Matrix science)  
637 against the Araport11 database. The target-decoy option of Mascot was enabled and search  
638 parameters included a precursor tolerance of 1.3 Da and a fragment ion tolerance 0.45 Da.  
639 Enzyme specificity was set to trypsin and up to two missed cleavages were allowed. The  
640 Mascot <sup>13</sup>C option, which accounts for the misassignment of the monoisotopic precursor peak,  
641 was set to 1 and oxidation of methionine and carbamidomethylation of cysteines were included  
642 as variable and fixed modification, respectively. The isobarQuant workflow was used to  
643 generate protein identification files <sup>67</sup>.

#### 644 ***Spectra validation***

645 sORF peptides identified by database searching that could not be mapped to an existing  
646 Araport11 gene model were synthesized at JPT Peptide Technologies (Berlin, Germany) using  
647 Fmoc-based SPOT synthesis on membranes <sup>59</sup> and measured on the same mass spectrometer  
648 that was used for data acquisition (Tissue atlas full proteome method; see above for method  
649 description). Experimental and synthetic peptide spectra were extracted from the raw files and  
650 used for similarity calculation without prior processing. Normalized spectral contrast angle (SA)  
651 comparison between spectra of the tissue sample and synthetic peptides was performed using  
652 in-house R scripts <sup>68</sup> factoring in peaks which are either shared between spectra or exclusive to  
653 the synthetic peptide spectra. Peaks exclusive to experimental spectra were ignored.  
654 Candidates were selected with SA angle cutoff larger than 0.7 and BLASTed against the  
655 UniProt database for further validation (Supplementary Data 3).

656 Protein identifications for the 'uncertain' evidence category of UniProt were validated by  
657 comparing the experimental spectra to in-silico predicted fragment spectra (Supplementary  
658 Table 1) <sup>12</sup>. For this, a spectral library was obtained from Prosit  
659 (<https://www.proteomicsDB.org/prosit>) <sup>12</sup> by uploading all sequence-charge combinations of  
660 peptides that were identified for 'uncertain' proteins. To obtain the best matching spectra, the  
661 collision energy of Prosit was calibrated using a standard quality control run from the same  
662 mass spectrometer that was used for data acquisition. The resulting predicted spectral library

663 was visualized and compared to the experimentally acquired data analog to the sORF candidate  
664 peptides. SA values larger than 0.7 were used as cutoff.

### 665 ***RNA sequencing***

666 Total RNA was isolated with the NucleoSpin RNA Plant kit (Macherey-Nagel, Düren, Germany)  
667 according to the manufacturer's instructions. DNA was removed by on-column treatment with  
668 rDNAse (Macherey-Nagel, Düren, Germany). For recalcitrant samples (seed, silique, pollen), a  
669 LiCl-based protocol was adopted with minor modifications<sup>69</sup>. After LiCl precipitation, the RNA  
670 pellet was dissolved in rDNAse buffer and treated with rDNAse (Macherey-Nagel, Düren,  
671 Germany) at 37°C for 10 min. The final pellet was re-suspended in 35 µl DEPC-treated water.

672 RNA was quantified (Nanodrop<sup>TM</sup>, Thermo Fisher Scientific, Waltham, USA ) and quality  
673 checked with a Bioanalyzer 2100 (Agilent Technologies, Santa Clara, USA). RNA integrity  
674 number (RIN) values between 6.4 and 10 were accepted for further analysis. cDNA libraries  
675 were prepared using the TruSeq Stranded mRNA Sample Preparation kit (Illumina, San Diego,  
676 USA) according to the instructions. Clusters were generated in two batches and sequenced on  
677 a High throughput flow cell with the HiSeq 2500 platform (Illumina, San Diego, USA) to a depth  
678 of 36 million reads per sample. Quality assessment of raw and trimmed 75 bp paired RNA-seq  
679 reads was performed with FastQC. Raw RNA-seq reads were trimmed to remove adapter  
680 contamination and poor quality base calls using Trimmomatic version 0.35 with parameters  
681 (ILLUMINACLIP: Illumina-PE.fasta:2:30:10; LEADING:3; TRAILING:3; SLIDINGWINDOW:4:20;  
682 MINLEN:36)<sup>70</sup>. Trimmed RNA-seq reads were mapped to the Araport11<sup>4</sup> transcriptome with  
683 Kallisto version 0.43.1 (default parameters)<sup>71</sup>.

### 684 ***Data processing***

685 MaxQuant output tables were filtered for non-plant contaminants, reversed sequences and  
686 proteins which were only identified based on modified peptides. Protein abundance estimation  
687 was based on either intensity-based absolute quantification (iBAQ)<sup>26</sup>, or top3 quantification<sup>72</sup>,  
688 depending on the analysis. MaxQuant ProteinGroups containing several gene loci were filtered  
689 out in order to retain only unambiguously identified gene loci for further analyses. In case  
690 multiple protein isoforms were identified in distinct ProteinGroups, only the isoform with the  
691 higher number of razor+unique peptides was retained.

692 mRNA quantities are displayed as transcripts-per-kilobase-million (TPM) and a cutoff of 1 TPM  
693 was used as lower limit of detection across all samples. Gene ontology<sup>73</sup> (GO)-term analysis for  
694 the transcript abundance range was performed using the 1D enrichment function from Perseus

695 <sup>74,75</sup> with Benjamini-Hochberg FDR threshold set to 0.01. In this function, a two-sided Wilcoxon-  
696 Mann-Whitney test is employed to test for systematically larger or smaller transcript abundance  
697 within a GO category as compared to the global distribution of all values (Supplementary Data  
698 4).

699 For further qualitative and quantitative analyses, all transcript or protein isoform information was  
700 collapsed onto gene level. Unless otherwise stated, displayed abundances for protein, transcript  
701 and phosphorylation sites (p-site) were  $\log_2$  transformed. Protein, peptide and transcript  
702 datasets for the tissue map and seed treatment experiments were median centered to the  
703 overall median of the respective dataset. No normalization was performed for the p-site dataset,  
704 since total p-site intensity variations between tissues are also due to biological sample  
705 differences. Instead, the spike-in phosphopeptide library was used, to assess reproducible  
706 enrichment efficiency and MS measurement quality of phosphoproteome samples <sup>56</sup>.

707 Phosphorylation sites (p-sites) which were reported in the MaxQuant output table  
708 (Phospho(STY)sites.txt file) with a 'localization probability' larger than 0.75 were designated as  
709 'high confidence localizations' or class I sites <sup>76</sup>. P-sites were considered exclusive if they were  
710 only detected in a single tissue. The number and identity of p-sites and phosphoproteins  
711 detected in this study were compared to datasets available through PhosPhAT4.0 and a  
712 published meta-analysis <sup>8,9</sup> (Extended Data Fig. 1h).

### 713 **Data analysis**

714 **Genome annotations:** Chromosome information contained in the Arabidopsis locus identifiers  
715 (AGI codes: AT [Arabidopsis thaliana]; 1, 2, 3, 4, 5, M, C [chromosome number, M for  
716 mitochondrial, C for chloroplast]; G [gene]; 12300 [five-digit code for position on chromosome]),  
717 was used to assign genes to their respective chromosomes (Extended Data Fig.1c). Araport11  
718 gene identifiers (Arabidopsis gene identifiers [AGI]) were mapped to the UniProt *Arabidopsis*  
719 *thaliana* reference proteome (taxon identifier 3702; UP000006548; download 11/2018) based on  
720 protein sequence. Swiss-Prot, TrEMBL as well as protein existence criteria annotations (level1:  
721 evidence on protein level; level2: evidence on transcript level; level 3: inferred from homology,  
722 level 4: predicted, level 5: uncertain) were subsequently obtained from UniProt (Extended Data  
723 Fig.1d).

724 N- and C-terminal peptide sequences were extracted from the MaxQuant peptides.txt file and  
725 filtered for zero missed cleavages (n = 2,776) (Extended Data Fig. 2a). N-terminal peptides  
726 were divided into groups with (n = 1,707) or without (n = 1,069) cleavage of the initiator

727 methionine. The frequency of the 20 genetically encoded amino acids at the position after the  
728 start codon was subsequently calculated separately for both groups and displayed as a pie  
729 chart. For N-terminal peptides with the same amino acids at the position after the start codon,  
730 the percentage of peptides with N-terminal acetylation was also calculated and displayed as bar  
731 plot. This analysis was also performed separately for the groups with or without cleavage of the  
732 initiator methionine (Extended Data Fig. 2b,c).

733 Gene isoforms annotated in Araport11 were considered as 'identified', if they were detected with  
734 a TPM intensity larger than our limit of detection cutoff (1 TPM; transcript level) or with an  
735 isoform-specific peptide (protein level) in at least one tissue sample (Extended Data Fig. 2f,  
736 Supplementary Data 3). A selection of isoform-specific peptides was synthesized together with  
737 the sORF peptide collection at JPT Peptide Technologies (Berlin, Germany) and the synthetic  
738 peptides were used for validation of the experimental spectra identifications as described above.

739 Transcription factor, transcription regulator, kinase and phosphatase family annotations and  
740 classifications are based on reports by Zheng et al.<sup>16</sup> and Yang et al.<sup>17</sup>. Proportional coverage  
741 of these families within our dataset was calculated by counting how many of them could be  
742 identified on transcript, protein or phosphoprotein level, respectively (Extended Data Fig. 2k).

743 ***Tissue groups and tissue characteristics:*** Tissue samples were assigned to tissue groups as  
744 follows, based on their origin or common morphology: flower (sepal, petal, stamen, carpel,  
745 silique, flower); fruit (silique septum, silique valves); seed (embryo, seed, seed imbibed); pollen  
746 (pollen); leaf (cauline leaf, leaf distal, leaf proximal, leaf petiole, senescent leaf, cotyledons,  
747 shoot tip); stem (node, internode, flower pedicle, hypocotyl); root (root, root tip, root upper  
748 zone); callus (egg-cell like callus, callus); cell culture (cell culture early, cell culture late) (Fig.  
749 1a,b).

750 To provide a measure of tissue similarity, the Pearson correlation coefficient was calculated for  
751 the gene expression of all pair-wise tissue combinations. The Pearson correlation coefficient is  
752 a measure of the linear correlation between two variables, in this case the expression levels in  
753 two tissue samples. Correlations were computed both on protein level and transcript level and  
754 displayed as separate heatmaps for both omics levels (Extended Data Fig. 1a). For three  
755 examples of morphologically highly similar tissue pairs, the gene expression levels were also  
756 displayed as scatter plots using protein abundance or transcript abundance measurements,  
757 respectively (Extended Data Fig. 1b).



758 Tissue or tissue group specificity of genes was calculated based on iBAQ or TPM abundance  
759 values, respectively <sup>77</sup>. Genes were assigned to categories in the following order: 'tissue  
760 specific', 'tissue enhanced', 'group-specific', 'group-enhanced', 'shared' and 'mixed'. Genes  
761 were considered 'specific', if they were only detected in a particular tissue or tissue-group and  
762 'enhanced' if their abundance was at least five-fold higher in a particular tissue or tissue-group  
763 as compared to the average levels in all other tissues. Genes that were detected in all 30  
764 tissues but did not show enhanced expression in a tissue or tissue group were classified as  
765 'shared'. All remaining genes are contained in the 'mixed' category (Extended Data Fig. 3a).

766 Genes detected in all tissues on either protein or transcript level were assigned to the core  
767 datasets (core\_transcript n= 8,405; core\_protein n = 7,734; core\_intersection n = 5,043). This  
768 classification does not consider gene expression levels and should not be confused with the  
769 tissue-specificity classification described in the previous paragraph.

770 Hierarchical clustering analysis for tissues representing flower parts or the whole flower was  
771 performed on log<sub>2</sub>-transformed, z-scored protein intensities (iBAQ values) in Perseus using  
772 Euclidean distance and average linkage (Extended Data Fig. 3b). The flower organ identity  
773 model was restricted to the simplified ABC model, thus only displaying homeotic genes for the  
774 A, B and C classes <sup>78</sup>, namely the expression of MADS-box transcription factors *APETALA1*  
775 (*AP1*) for class A, *APETALA3* (*AP3*) and *PISTILLATA* (*PI*) for class B and *AGAMOUS* (*AG*) for  
776 class C. Class A expression specifies sepal formation, the combination of class A and B  
777 specifies petal formation, the combination of class B and C specifies stamen formation and  
778 class C expression specifies carpel formation in developing flowers.

779 For the cumulative abundance calculation of five representative tissues (flower; pollen; root tip;  
780 leaf proximal; seed), proteins (iBAQ) and transcripts (TPM) were first ranked from highest to  
781 lowest individual intensity (Extended Data Fig. 3e). The running total was then plotted against  
782 the rank order. The names or identifiers of the five most abundant transcripts or proteins (rank 1  
783 to 5) are listed in descending order for the respective tissue. Shared IDs among the top 100  
784 most abundant transcripts (TPM) and proteins (iBAQ) were calculated for each individual tissue  
785 (Extended Data Fig. 3f). For the genes representing the highest abundant protein in at least one  
786 tissue, the contribution to the total protein amount in an individual tissue was calculated by  
787 dividing the iBAQ intensity (not log transformed) of the respective protein by the summed total  
788 iBAQ intensity (not log transformed) in this tissue (Extended Data Fig. 3g).

789 Principal component analysis (PCA) of proteome and transcriptome data was performed in  
790 Perseus for the intersection of the core datasets (n = 5,043) on log<sub>2</sub>-transformed and z-scored

791 iBAQ and TPM intensities (Extended Data Fig. 3h). Subcellular localization information was  
792 downloaded from SUBA (download 11/2016; unambiguous localizations  $n = 3,506$ )<sup>44</sup>  
793 (Supplementary Data 2) and used to calculate the intensity contribution of proteins assigned to  
794 a specific compartment for the different tissue groups. For this, the percentage of proteins with  
795 the same SUBA annotation was calculated by dividing the summed protein intensity (iBAQ, not  
796 log transformed) of each SUBA category by the total summed iBAQ intensity (not log  
797 transformed) within each tissue. To compare tissue groups, the respective protein intensity  
798 proportion was then averaged for all tissues within one group. These averaged proportions were  
799 subsequently plotted for each subcellular compartment (Extended Data Fig. 3i).

800 **Protein/mRNA relation:** The Pearson correlation value between median protein (median iBAQ  
801 of 30 tissues) and median transcript (median TPM of 30 tissues) abundances was calculated  
802 using the set of genes with abundance measurements on both protein and transcript level in  
803 more than ten tissues (more than 10 pairwise complete observations;  $n = 14,069$ ). The  
804 scatterplot of median transcript (TPM) and protein abundance (iBAQ) was displayed together  
805 with their marginal histograms (Fig. 2a). Tissue-specific Pearson correlation values between  
806 protein and transcript abundance were calculated using all genes from the core proteome and  
807 core transcriptome intersection dataset ( $n = 5,043$ ; Extended Data Fig. 4a). The core dataset  
808 was used here to base the Pearson correlation value comparison between tissues on the same  
809 set of genes in all tissues.

810 The data subset with more than 10 pairwise complete observations on protein and transcript  
811 level ( $n = 14,069$ ) was also used for all further calculations involving protein-to-mRNA ratios  
812 (PTR) (Fig. 3d, Extended Data Fig. 5). PTR values are calculated by building the ratio between  
813 protein abundance (iBAQ) and the corresponding transcript abundance (TPM) for each gene  
814 and were calculated separately for each tissue. The tissue PTR values were then used to  
815 calculate the median and median absolute deviation (MAD) of PTR values across all 30 tissues  
816 (Extended Data Fig. 5). The variation of PTR values across tissues indicates, whether protein  
817 and transcript levels of a given gene are regulated in a similar (small PTR variation) or different  
818 way (high PTR variation) between individual tissues. To estimate the proportion of genes with  
819 rather stable or variable PTR values, the PTR MAD values were distributed into five equal parts,  
820 so that 20% of all genes from this analysis are contained in one part (5 MAD quantiles: Q1-Q5).  
821 For each gene, the median PTR values were plotted against their MAD across tissues and the  
822 MAD quantiles indicated in the plot (Extended Data Fig. 5a). GO-term analysis for the median  
823 PTR distribution (median PTR across all tissues) was performed using the 1D enrichment

824 function from Perseus <sup>74</sup> with Benjamini-Hochberg FDR threshold set to 0.01 (Supplementary  
825 Data 4). In this function, a two-sided Wilcoxon-Mann-Whitney test is employed to test for  
826 systematically larger or smaller PTR values within a GO category as compared to the global  
827 distribution of all values.

828 In a similar way, the variation of phospho ratios across tissues indicates, whether p-site levels  
829 are driven by protein abundance (small phospho ratio variation) or p-site stoichiometry (high  
830 phospho ratio variation) changes, respectively. Phospho ratios were calculated by building the  
831 ratio between a p-site abundance (intensity) and the abundance of its corresponding protein  
832 (iBAQ). For this, we used the set of p-sites, with abundance measurements on both p-site and  
833 protein level in more than ten tissues (more than 10 pairwise complete observations; n =  
834 13,793). Phospho ratios were calculated separately for each tissue and subsequently combined  
835 to calculate the median phospho ratio and phospho ratio MAD across all 30 tissues. To estimate  
836 the proportion of p-sites which closely resemble the protein abundance profile, the phospho  
837 ratio MAD values were again distributed into five equal parts (5 MAD quantiles: Q1-Q5), and the  
838 median phospho ratio values plotted against their MAD across tissues each p-site. MAD  
839 quantiles were indicated in the plot (Extended Data Fig. 5c).

840 To provide further information about inter-tissue variability, MAD quantiles were also calculated  
841 and displayed for the expression levels on protein (iBAQ; n = 14,069), transcript (TPM; n =  
842 14,069) and p-site (peptide intensity; n = 13,793) levels, respectively (Extended Data Fig. 5b,d).

843 **Features for protein level prediction models:** Since a substantial proportion of variation in  
844 protein levels remained unexplained when using transcript level information alone (Pearson  
845 correlation between protein and transcript abundance in tissues 0.28-0.79), additional molecular  
846 features, that could explain protein abundance variations, were tested for their influence on  
847 protein abundance in a model selection approach. Predictors selected for this analysis were:  
848 mRNA levels, codon usage, non-synonymous to synonymous substitutions (*Dn/Ds*) ratios,  
849 which are a measure of evolutionary conservation, gene/coding sequence (CDS) length, exon  
850 number, gene position on the chromosome, cytosine methylation, the number of putative protein  
851 interactions and mRNA sequence motifs (kmers of size 3 to 7 nucleotides):

852 Codon usage statistics for the *A. thaliana* genome were obtained from Kazusa  
853 ([www.kazusa.or.jp/codon/current/species/3702](http://www.kazusa.or.jp/codon/current/species/3702)) and parsed to extract NCBI gene identifiers.  
854 These identifiers were mapped to their corresponding UniProt entries and Ensembl/TAIR10  
855 annotations using the UniProt Retrieve/ID mapping tool. The extracted TAIR10 annotation was

856 merged with the Kazusa codon usage dataset. Codon frequencies were calculated for each  
857 gene by dividing the count (x 3) of a given codon by the full length of the coding sequence.

858 The *Dn/Ds* substitution rates were calculated from CDS pairs between *Arabidopsis thaliana* and  
859 its closest relative *Arabidopsis lyrata*. Reciprocal best BLAST with an e-value cutoff of  $\leq 1E-08$   
860 was used to identify ortholog sequences. Individual CDS pairs were aligned using PRANK<sup>79</sup>  
861 and Gblocks<sup>80</sup> was applied to eliminate poorly aligned positions in an alignment with a cutoff of  
862 8 contiguous non-conserved positions and without allowing for gap positions. The yn00 package  
863 in the program PAML<sup>81</sup> for pairwise sequence comparison was used to estimate substitution  
864 rates, *Dn* and *Ds*, respectively.

865 The total number of exons and the total gene lengths were obtained from Araport11. The  
866 distance of each gene from the chromosomal centromeres were calculated to capture potential  
867 position-specific effects.

868 *A. thaliana* (Col-0) Whole Genome Bisulphite Sequencing (WGBS) data was obtained from van  
869 der Graaf et al. 2015<sup>82</sup>. For each gene, methylation levels were calculated for contexts CG,  
870 CHG and CHG (where H = adenine, cytosine, thymine) separately. Per gene methylation levels  
871 were defined as:

$$g_i = \frac{1}{\max(j)} \times \sum \frac{Nm_j}{N_j}$$

872 Here,  $\max(j)$  is the total number of cytosines,  $Nm_j$  is the number of methylated reads and  $N_j$  the  
873 total number of reads at the  $j$ th cytosine.

874 Arabidopsis protein-protein interactions were downloaded from STRING<sup>30</sup> and the number of  
875 protein interaction partners extracted for each gene.

876 All of these features have previously been associated with transcriptional activity and/or protein  
877 abundance levels in Arabidopsis and/or other species<sup>83-88</sup>. For a detailed feature set description  
878 see Supplementary Data 5.

879 ***De novo motif identification:*** Motifs in the mRNA CDS, 3' or 5'UTR region were identified as  
880 previously described<sup>23</sup>. Briefly, protein expression levels were  $\log_{10}$  transformed and median  
881 centered. For genes with two or more transcript isoforms, the transcript isoform reported to have  
882 the largest summed iBAQ values across all tissues was defined as the major transcript isoform  
883 per gene and used to compute all sequence feature and mRNA levels. Raw RNA-seq reads  
884 were trimmed to remove adapter contaminations and poor quality base calls using Trimmomatic

885 0.39 with parameters (ILLUMINACLIP:illumina-PE.fasta:2:30:10; LEADING:3; TRAILING:3;  
886 SLIDINGWINDOW:4:20; MINLEN:36). Trimmed RNA-seq reads were mapped to the Araport11  
887 transcriptome annotation with Kallisto version 0.46.0 using default parameters. To estimate the  
888 levels of mature mRNA, the number of reads mapping to exonic and intronic regions of the  
889 transcripts were counted separately and then normalized by the total exonic and intronic region  
890 lengths, respectively. Normalized intronic counts were subtracted from the normalized exonic  
891 counts to obtain the mature mRNA counts. The resulting normalized exonic counts per sample  
892 were corrected by the DESeq2<sup>89</sup> library size factor and log<sub>10</sub> transformed. Transcripts with 10  
893 reads per 1kb were treated as transcribed. Tissue-specific protein-to-transcript ratios (PTR)  
894 were computed using the normalized protein and transcript levels. GEMMA software<sup>90</sup> was  
895 used to identify de-novo motifs in 5'UTR, CDS and 3'UTR regions using the tissue-specific  
896 PTRs as response variable. GEMMA uses a linear mixed model, in which the effect of each  
897 individual kmer on the median PTR across tissues is assessed while controlling for the effect of  
898 other kmers (random effects), region length and GC percent (fixed effects). The motif search  
899 was performed for kmers ranging from 3-7 nucleotides. Obtained p-values were adjusted for  
900 multiple testing with Benjamini-Hochberg's false discovery rate (FDR) and jointly computed  
901 across the p-values of all tissues. Gemma was run using the median PTR with FDR<0.1 and  
902 covariates set to 'false'. 82 significant putative motifs were obtained based on their sequence  
903 (5'UTR n = 32; 3'UTR n = 38; CDS n = 12) and sub-sequence (initial, all, end) region. 39 motifs  
904 that lie in the 'initial' and 'end' sub-sequences were further selected. The presence or absence  
905 of each enriched motif with respect to each gene was extracted in form of a binary matrix and  
906 used for downstream multivariate feature selection analysis.

907 **Model-based feature selection:** Tissue-specific protein expression data was merged to the  
908 feature matrix. Preliminary pair-wise correlation analysis showed only weak to moderate  
909 correlation between individual features. In addition, Variance Inflation Factors (VIF) were  
910 calculated for each feature using the fmsb R package<sup>91</sup>. The result showed low VIFs,  
911 suggesting that multicollinearity was not an issue for downstream analyses.

912 Two model selection approaches were implemented, stepwise regression and Lasso regression  
913<sup>92,93</sup>. To select the most predictive features for protein abundance in each tissue, we used a  
914 forward-backward model selection approach in a multiple regression framework. The method  
915 was implemented using stepwiseAIC() function in R<sup>94</sup>, which compares the fit of nested models.  
916 To ensure that the comparison of model AICs were not affected by unequal sample size,  
917 missing data were removed prior to the analysis.

918 Because stepwise regression can occasionally lead to over-fitting<sup>95</sup>, a Lasso regression was  
919 implemented as an alternative model selection procedure. Lasso regression performs L1  
920 regularization, which adds a penalty equivalent to the absolute of the magnitude of regression  
921 coefficients and tries to minimize them. The strength of the penalty was controlled via the tuning  
922 parameter  $\lambda$ <sup>93</sup>. Lasso was implemented using the glmnet package<sup>96</sup> in R. Model training was  
923 performed on a random selection of genes (50% of the dataset) and implemented using the  
924 cv.glmnet() function. The optimal value for  $\lambda$  was extracted and used to re-build the model using  
925 the glmnet() function. Finally, the fitted model was used to obtain predictions in the remaining  
926 50% of the genes.

927 For each tissue, stepwise and Lasso regression models were compared. Stepwise regression  
928 yielded only slightly higher coefficients of determination ( $R^2$ ) values compared to Lasso,  
929 suggesting over-fitting was not an issue (Supplementary Data 5). As stepwise regression  
930 yielded more parsimonious models in general, we used this approach for further analysis.  
931 Selected features here could explain on average 52% of protein abundance variation (37% in  
932 pollen, 62% in cell culture early) (Supplementary Data 5). For each tissue, features from the  
933 best fitting models were summarized in an incidence matrix along with the effect direction  
934 (positive or negative effect on protein levels). To determine the importance of each feature to  
935 the overall model fits,  $R^2$  variance decomposition was performed using the 'genici' metric which  
936 is implemented in the relaimpo R package<sup>97</sup> (Extended Data Fig. 4c). Relative feature  
937 contributions were averaged across all tissues (Fig. 3b).

938 Since many of the detected motifs appear in a tissue-specific manner (predictive only in tissue  
939 subset), we clustered tissues according to the presence or absence status of 5'UTR motifs in  
940 each tissue model (Extended Data Fig. 4d). Seed and pollen tissues form a distinct subcluster,  
941 which might be connected to the increased/decreased PTR levels in these tissues compared to  
942 the other tissues (Fig. 3c; Extended Data Fig. 4a). In contrast to the motif analysis, Dn/Ds ratios  
943 were consistently (and positively) associated with protein abundance in all 30 tissues  
944 (Supplementary Data 5). To explore the relationship between Dn/Ds ratios and protein  
945 abundance in more detail, groups of genes with low or high (bottom 5% or top 5% of Dn/Ds  
946 distribution) were compared to each other with regard to protein levels (Extended Data Fig. 4e).

947 **Seed tissue PTR regulation:** The PTR value distribution was plotted for the median PTR  
948 (median across all tissues, see above) and selected tissues (seed, seed imbibed, pollen, cell  
949 culture young). Seed and pollen tissues show particularly low Pearson correlation between  
950 protein and transcript abundance levels (Extended Data Fig. 4a). Cell culture early in

951 comparison shows the highest Pearson correlation among the analyzed tissues. Tissue-specific  
952 'outliers' with especially high or low PTR as compared to all other tissues were selected if their  
953 PTR value was outside two standard deviations of the mean of the median PTR distribution. For  
954 seed, this resulted in 469 genes with 'high' and 571 genes with 'low' PTR. In order to interpret,  
955 whether this change in seed PTR values was caused by differential regulation on transcript  
956 and/or protein level, the fold change between seed protein and transcript abundance and the  
957 median protein and transcript abundance of all tissues was calculated. Genes with at least  
958 4fold-change in either protein or transcript abundance were considered regulated (less/more  
959 transcript and/or less/more protein in seed compared to all tissues). The percentage of genes  
960 with high or low PTR levels in the seed tissue, which are regulated in the same manner  
961 (less/more transcript and/or protein) was calculated and displayed as arrow plot (Fig. 3e). About  
962 a quarter of each gene set (high PTR 27%; low PTR 24%) show no regulation based on our  
963 4fold-change cutoff.

964 For the low PTR gene set, a high proportion of genes with lower protein abundance in the seed  
965 tissue was observed. A protein level chase experiment was performed, to investigate whether  
966 this reduction was due to translational inhibition or increased protein degradation in seeds.  
967 Protein level (iBAQ, not log transformed) fold changes in CHX, MG132 and DMSO-treated  
968 samples were calculated relative to the baseline protein expression at 0h (control sample). The  
969 average protein level fold change for the subset of genes with either high or low PTR in seeds  
970 (see above) was subsequently determined for each time point and plotted separately for 'high'  
971 and 'low' PTR genes (Fig. 3f). To test for significant fold change differences between treatment  
972 time points, a one-way analysis of variance (ANOVA) and post-hoc Tukey HSD test was  
973 performed using the stats package in R (Extended Data Fig. 4i). For this, the data was  
974 normalized for changes in the proteome caused by seed germination, by calculating the log<sub>2</sub>  
975 fold change in protein abundance (iBAQ) between seed samples treated with cycloheximide  
976 (CHX) or MG132 and the time-point matched DMSO control. Outlier values were removed for  
977 the boxplot visualization but are included in the ANOVA and post-hoc Tukey analysis.

978 **Co-expression analysis:** To compare gene co-expression information in our dataset to prior  
979 knowledge about various associations between genes pairs, the Pearson correlations between  
980 all pair-wise gene combinations on both transcript and protein level (core dataset intersection; n  
981 = 5,043) was calculated. The correlation coefficient value for a given gene pair on transcript  
982 level was then plotted against the correlation coefficient value of the same pair on protein level  
983 (Extended Data Fig. 6a). Protein-protein association data was downloaded from STRING <sup>30</sup>

984 (www.string-db.org; 3702.protein.links.detailed.v10.5.txt.gz; download 07/2018), the  
985 experimental STRING subscores calculated for each gene pair and the information merged to  
986 the correlation value matrix. The scatterplot of transcript level versus protein level correlations  
987 was then divided into 50 x 50 bins along the x- and y-axis and the mean experimental STRING  
988 subscore for all gene pairs within a bin was calculated. Mean subscores were  $\log_2$  transformed  
989 and visualized as a heatmap together with their marginal histograms (Extended Data Fig. 6a).

990 For a subset of genes, pair-wise co-expression was further investigated. Pairs used in this  
991 analysis were genes, that are either annotated as duplicated<sup>31</sup> or as protein interactors (AtPIN  
992<sup>33</sup>, download 08/2017), respectively. The Pearson correlation between the expression levels of  
993 gene-pairs across tissues was calculated for gene pairs with abundance measurements in more  
994 than ten matching tissues on both protein and transcript level (more than 10 pairwise complete  
995 observations). The duplicated gene set was further filtered for 3 unique peptide identification of  
996 each paralog. Top3 intensities were used as protein abundance measure for the duplicate gene  
997 set since the subsequent ratio comparison was also performed with top3 intensities. Paralog  
998 genes often have high sequence identity on amino acid level, which can lead to distorted ratios  
999 due to uneven assignment of shared (razor) peptides to only one of the paralogs. Duplicated  
1000 genes (n = 3,612) were divided into three subsets: duplications caused by a whole genome  
1001 duplication event (WGD, n = 2,104), local duplication (local, n = 408) or transposon-mediated  
1002 duplication (transposed, n = 1,100). For each subset the distribution of Pearson correlation  
1003 values between duplicates on either transcript or protein levels was plotted (Extended Data Fig.  
1004 6b). A set of random gene pairs (n = 27,353) was generated for comparison, filtered like the  
1005 duplicated gene set (number of pairwise complete observation, 3 unique peptides) and the  
1006 Pearson correlation value distribution displayed in the same way. To compare relative protein  
1007 expression levels between paralogs, the ratio between the protein abundance (top3) of one  
1008 paralog and the protein abundance (top3) of the other paralog was calculated (Extended Data  
1009 Fig. 6c). As an example for the intensity proportion of paralog genes in different tissues, the  
1010 top3 intensity (not log transformed) of MAC5A and MAC5B was plotted as proportion of the  
1011 summed top3 intensity (not log transformed) of both paralogs (Extended Data Fig. 6c). For 57  
1012 paralog gene pairs with phenotypic information about asymmetric loss-of-function mutant  
1013 combinations<sup>32</sup>, we build the average top3 intensity proportion of the first paralog  
1014 ( $\text{dupl1}/(\text{dupl1}+\text{dupl2})$ ) across 30 tissues and plotted them in descending order together with the  
1015 phenotype information (Extended Data Fig. 6d).



1016 A set of well-studied, stable protein complexes (26S proteasome, COP9 signalosome,  
1017 Chaperonin, Cellulose synthase) was selected to estimate the protein level (iBAQ) co-  
1018 expression expected for stable interaction partners. For this, the Pearson correlation coefficient  
1019 values between all pair-wise subunit combinations of an individual complex were calculated and  
1020 displayed in a density plot (Extended Data Fig. 6e). Based on this analysis, a Pearson  
1021 correlation coefficient cutoff of >0.5 was subsequently used as indication for stable protein  
1022 interactions. The protein interactor gene set (AtPIN) was used to test the recovery of annotated  
1023 protein-protein interactions based on co-expression data from this study. Again, the distribution  
1024 of Pearson correlation values between gene pairs (here interactors) on either transcript or  
1025 protein level (iBAQ) was plotted. This was done for the whole AtPIN dataset (n = 57,152) and  
1026 the following subsets: interactions identified by yeast-two hybrid experiments (Y2H, n = 7,621),  
1027 by affinity-purification mass spectrometry (AP-MS, n = 17,982) or by both Y2H and AP-MS (n =  
1028 829).

1029 **Size exclusion chromatography and complex analysis:** Reproducibility between the three  
1030 SEC experiments was tested by comparing the elution behavior of the same proteins. The  
1031 coefficient of determination between protein peaks in the different experiments was above 0.7  
1032 (flower-root  $R^2 = 0.82$ ; flower-leaf  $R^2 = 0.78$ ; root-leaf  $R^2 = 0.7$ ). Protein peak elution between  
1033 the samples was also consistent across the whole SEC gradient range (Extended Data Fig. 7b).

1034 To assign proteins to potential complexes, peak correlation profiling was performed. For this,  
1035 the R package CCprofiler v0.1 was used to analyze the peptides.txt output table from MaxQuant  
1036 <sup>62,98</sup>. Peptide table entries were restricted to the maximum molecular weight per gene name for  
1037 the quantification of protein groups. This step removed peptides mapping to smaller isoforms of  
1038 each gene. The restricted proteinGroups.txt served as the trace annotation input table for  
1039 CCprofiler. The calibration table of the SEC column was based on the high molecular weight gel  
1040 filtration calibration kit (GE Healthcare, Chicago, USA). The peptides table was split into the  
1041 different tissues and the resulting tables converted into the input format for CCprofiler. All  
1042 subsequent steps were performed separately for each tissue table.

1043 The peptides table was imported, converted into a traces object, where a trace object is the  
1044 SEC-elution profile of a specific peptide and annotated with the corresponding fractions and  
1045 additional external information (e.g. molecular weight of the respective fraction, molecular  
1046 weight of the respective protein) based on the aforementioned calibration and restricted  
1047 proteinGroups tables. Traces not containing at least three consecutive peptide identifications  
1048 across fractions, as well as traces with a sibling peptide correlation of less than 0.2 between

1049 peptides originating from the same protein were filtered out. Based on the remaining traces,  
1050 protein features (elution peak positional information) consisting of highly correlated peptides  
1051 (correlation higher than 0.9) were detected using CCprofiler's sliding window algorithm.  
1052 Peptides were randomly assigned to proteins in order to control the false discovery rate of  
1053 protein features at 5% (random decoy model). Subsequently, protein traces were calculated by  
1054 summing up the intensities of the top two most abundant peptide traces.

1055 Next, complex hypotheses consisting of target and decoy protein complexes were constructed  
1056 based on a previously-published mapping of Arabidopsis orthologues to mammalian protein  
1057 complexes from CORUM<sup>99,100</sup>. Proteins were only mapped to the same decoy complex if they  
1058 were not interacting with each other directly (minimum path length of two). These target and  
1059 decoy complexes were used during the detection of complex features consisting of highly  
1060 correlated proteins using the same sliding window algorithm as above in order to control the  
1061 false discovery rate of complex features at 5% (target-decoy model).

1062 Both protein features (elution peak positional information) and protein traces (quantitative  
1063 information) were then used to generate an input matrix for weighted gene correlation network  
1064 analysis (WGCNA)<sup>101</sup>, which was used to find clusters of proteins with correlated SEC elution  
1065 profiles. Protein traces were restricted to the ones, which were part of at least one protein  
1066 feature. Each protein trace was duplicated for each protein feature it was part of and all  
1067 intensities outside of the respective protein feature were set to zero. With this, protein traces  
1068 were effectively split into separate elution peaks corresponding to distinct (sub)complexes.  
1069 Afterwards, elution peaks, which met either of the following criteria were filtered out: (1) The  
1070 absolute difference between the molecular weight at the apex of the elution peak and the  
1071 monomer molecular weight of the corresponding protein was smaller than twice the monomer  
1072 molecular weight. (2) The absolute difference between the molecular weight at the apex of the  
1073 elution peak and the monomer molecular weight of the corresponding protein was less than 200  
1074 kDa. (3) The apex of the elution peak was in fraction 77 (void fraction). (4) The apex of the  
1075 elution peak was in fraction 4 (monomer range).

1076 The remaining elution peaks were restricted to the intersection with the core protein dataset  
1077 across tissues described above (see section on tissue groups), generating the SEC WGCNA  
1078 input dataset. At the same time, an additional WGCNA input dataset was generated based on  
1079 the core protein dataset across tissues and restricted to the intersection with the SEC WGCNA  
1080 input dataset. Proteins with several SEC elution peaks were duplicated to match the SEC  
1081 WGCNA input dataset. WGCNA was carried out separately for each of these datasets. Signed

1082 co-expression similarities were calculated between all pairs of proteins with at least seven  
1083 pairwise-complete observations using the following formula:

$$s_{ij} = \frac{1 + \text{cor}(x_i, x_j)}{2}$$

1084 Here,  $s_{ij}$  is the signed co-expression similarity between two proteins  $x_i$  and  $x_j$  (based on their  
1085 Pearson correlation across tissues). Adjacency matrices were calculated with  $A = [s_{ij}]$  for  
1086 several values of  $\beta \in [1, 30]$ .

$$a_{ij} = s_{ij}^\beta$$

1087 Here,  $a_{ij}$  is the adjacency between two proteins  $x_i$  and  $x_j$ . The adjacency function parameter  $\beta$   
1088 was selected to be 30 for the construction of signed protein co-expression networks. The  
1089 topological overlap matrix  $\Omega = [\omega_{ij}]$  of the two networks was calculated with:

$$\omega_{ij} = \frac{l_{ij} + a_{ij}}{\min\{k_i, k_j\} + 1 - a_{ij}}$$

1090 Here,  $l_{ij} = \sum_u a_{iu} a_{uj}$  and  $k_i = \sum_u a_{iu}$ . Hierarchical clustering was performed on the topological-  
1091 overlap-based dissimilarity matrices  $D = [1 - \omega_{ij}]$  using average linkage. Correlation clusters  
1092 ('Modules') were detected using adaptive branch pruning<sup>102</sup> using the 'Dynamic Hybrid' method  
1093 set to respect the dendrogram topology during PAM operations and requiring at least 30  
1094 members per module. Similar clusters in the SEC or tissue dataset were merged, if the  
1095 dissimilarity of their module eigengenes was smaller than 1-MPC or 1-MTC, respectively. MPC  
1096 is the median peak correlation of the FDR-filtered complex features from CCprofiler (known  
1097 complexes), while MTC is the median tissue correlation of the very same complex features  
1098 (pairwise correlation between proteins mapping to a specific complex feature). The resulting  
1099 modules for both datasets were then mapped to each other using a combination of Fisher's  
1100 Exact test and manual curation. Enrichment of functional annotations from Corum<sup>100</sup>, GO<sup>73</sup>,  
1101 KEGG<sup>103</sup> and Reactome<sup>104</sup> were calculated in each cluster using Fisher's Exact Test. All p-  
1102 values were adjusted for multiple-testing by calculating FDRs<sup>105</sup> (Supplementary Data 8).

1103 In order to quantify how well complexes can be detected using the tissue atlas (TA) or SEC  
1104 WGCNA output, we calculated a summary statistic termed 'complex index'. Protein interactor  
1105 information was downloaded from UniProt<sup>6</sup> (<https://uniprot.org>; 12/2018) and manually curated  
1106 for the presence of large ( $> 4$  subunits) and small ( $\leq 4$  subunits) complexes (Extended Data Fig.  
1107 7e; Supplementary Data 9). The complex index (C) was calculated using the following formula:

$$C = \frac{S_m}{S} \times \frac{S_m}{M}$$

1108 Here,  $S_m$  is the number of subunits detected as present in the same module.  $S$  is the total  
1109 number of subunits identified in the restricted datasets for either SEC or TA experiments and  $M$   
1110 is the total number of entries in the respective module.  $C$  is a measure of how well complex  
1111 subunits co-occur (either by co-elution or by co-expression) and thus are detected in the same  
1112 module and also quantifies the resolution of the detection method (module size). The complex  
1113 index is 1, when all subunits of a complex are identified in the same module and no other  
1114 proteins are contained in the module.

1115 **Complex stoichiometry analysis:** Absolute SEC protein elution traces of selected complexes  
1116 (chaperonin, 26S Proteasome, CSN, CESA) were plotted using top3 intensities (not log  
1117 transformed). Relative subunit proportions or stoichiometry for selected protein complexes  
1118 within individual tissues of the TA dataset were calculated using top3 intensities (based on the 3  
1119 most abundant unique peptides). Top3 intensity rather than iBAQ intensity was used, in order to  
1120 avoid distorted ratios caused by shared (razor) peptide assignment. In the case of paralog  
1121 genes with high protein sequence similarity, peptides were not required to be unique for one  
1122 gene, but rather for one 'paralog group'. The three most abundant peptides within a paralog  
1123 group were then used for the top3 calculations.

1124 For the example of the coatomer complex, the relative proportion of paralog genes in different  
1125 tissues was calculated by plotting the top3 intensity (not log transformed, unique for gene) of  
1126 each paralog as proportion of the summed top3 intensity (not log transformed) of all paralogs  
1127 (Extended Data Fig. 7d). For the calculation of subunit stoichiometry ratios of selected  
1128 complexes (chaperonin, 26S Proteasome, CSN, CESA), the top3 intensity (not log transformed)  
1129 of a subunit was divided by the average top3 intensity (not log transformed) of all complex  
1130 subunits. Subunit ratios were first calculated for each tissue and subsequently averaged across  
1131 all 30 tissues (chaperonin, 26S Proteasome, CSN) or only across tissues where the respective  
1132 subunits are mainly expressed (CESA4/7/8: node, internode, silique septum, silique valves;  
1133 CESA1/3/6: all other) (Extended Data Fig. 7g).

1134 **Subnetwork extraction:** *De novo* network enrichment was performed to identify tissue- or  
1135 tissue group-specific subnetworks and to link them to a molecular function. In contrast to gene  
1136 set overrepresentation or gene set enrichment analysis<sup>106</sup>, this approach is suited to identify  
1137 previously uncharacterized functions from large-scale molecular interaction networks.  
1138 KeyPathwayMiner<sup>107</sup> was used to extract tissue- and tissue group-specific subnetworks from

1139 transcriptomics and proteomics datasets. To enrich subnetworks with proteins that deviate in  
1140 their expression from other tissues, we employed z-scored expression values. These reflect  
1141 how many standard deviations the expression in a given tissue is away from the expression  
1142 range found in all other tissues:

$$z_{x,g} = \frac{x - \mu_{x \setminus x}}{\sigma_{x \setminus x}}$$

1143 Here x is a specific tissue or tissue group of interest, g a gene  $\mu$  the mean and  $\sigma$  the standard  
1144 deviation. Based on the following rule, a one-column indicator matrix  $I(x,g)$  was constructed as  
1145 input for KeyPathwayMiner for each tissue or tissue group x:

$$I(x, g) = \begin{cases} 1 & \text{if } |z_{x,g}| > 2 \\ 0 & \text{else} \end{cases}$$

1146 Here each row corresponds to a gene g. STRING {Szkarczyk, 2017 #513} *A. thaliana* network  
1147 (v. 10.5, download 10/2018) was used as the molecular interaction network, considering only  
1148 high confidence interactions with a score > 900. Subnetworks extracted via KeyPathwayMiner  
1149 were made available for individual tissues or tissue groups as part of the ATHENA web  
1150 application.

1151 **Phosphorylation sites and motif analysis:** Serine (S), threonin (T) and tyrosine (Y) content  
1152 and p-site number of individual proteins was calculated based on the longest sequence in case  
1153 of ambiguous isoform identifications (Fig. 5a, Extended Data Fig. 8g). Likewise, the schematic  
1154 depiction of phosphorylation (p-site) localization in LATE EMBRYOGENESIS ABUNDANT (LEA)  
1155 and receptor-like kinase proteins was based on the p-site localization in the longest isoform  
1156 sequence (Extended Data Fig. 8h,i). Functional domain assignment for receptor-like protein  
1157 kinase (RLKs) sequences was done using smart ([http://smart.embl-](http://smart.embl-heidelberg.de/smart/batch.pl)  
1158 [heidelberg.de/smart/batch.pl](http://smart.embl-heidelberg.de/smart/batch.pl))<sup>106</sup> and p-sites were manually assigned to specific domains based  
1159 on their localization in the protein (Extended Data Fig. 8i).

1160 For motif analysis within our dataset, sequence windows of 15 amino acids centered on the  
1161 identified class I p-sites (15 mers) were assigned to a motif class of either 'proline-directed',  
1162 'acidic', 'basic' or 'other' by following a binary decision tree<sup>36</sup> (Extended Data Fig. 8d).  
1163 Assignment to these categories was done sequentially as follows: proline amino acid at position  
1164 -1 (Proline-directed), 5 or more aspartic acid (D) or glutamic acid (E) at position +1 to +7  
1165 (acidic), arginine (R) or lysine (K) at position -3 (basic), D or E at position +1,+2 or +3 (acidic), 2  
1166 or more R or K at position -6 to -1 (basic) and otherwise (other).

1167 P-sites with high confident localization scores (class I) were divided into S, T and Y p-site  
1168 datasets. Motif extraction was performed separately for each motif class category (proline-  
1169 directed, acidic, basic, other) using the motif-X algorithm, implemented in the rmotifX R package  
1170 <sup>35</sup> (Supplementary Data 10). Cutoff settings were: min-seq.= 30, pval.cutoff = 1e-6 (S and T  
1171 datasets); min-seq.= 10, pval.cutoff = 1e-5 (Y dataset). Motif-X calculates the fold-increase of a  
1172 respective motif in the 'foreground' (p-site dataset) compared to the 'background' dataset (non-  
1173 phosphorylated peptides). To avoid mass spectrometry-based residue biases, all peptides from  
1174 our dataset that contained an STY amino acid and had only been identified in non-  
1175 phosphorylated form were used as the background for all motif-X analyses (258,395  
1176 sequences). These peptide sequences were centered on STY and extended where necessary  
1177 along the N- and C-terminal window to generate 15 mers. Position weight matrix sequence  
1178 logos were drawn using the 'bits' method for amino acid sequences in the ggseqlogo R package  
1179 <sup>109</sup> (Extended Data Fig. 8e, Supplementary Table 2). The motif-X fold increase for S motifs was  
1180 plotted for motifs with 2, 3 and 4 fixed amino acid positions (Extended Data Fig. 8f).

1181 Published p-site motifs were retrieved from PhosPhAT4.0 <sup>9</sup> and the Human Protein Reference  
1182 Database <sup>110</sup> (HPRD; www.hprd.org) and divided into groups depending on the number of fixed  
1183 amino acid positions within the motif sequence. These motifs were subsequently matched to the  
1184 p-site or background dataset in order to calculate detection frequency and fold increase (p-  
1185 site/background dataset) of a reported motif (Supplementary Data 10).

### 1186 ***AGCVIII protein expression and mutant phenotypic characterization***

1187 For the relative expression analysis of AGC kinases across tissues, the AGC1 and AGC3  
1188 subfamilies of Arabidopsis AGCVIII kinases were selected <sup>21</sup>. The summed total intensity of  
1189 AGC1 and AGC3 subfamily kinases (top3, not log transformed) was calculated for each tissue.  
1190 Relative protein amounts of individual kinases in different tissues were calculated as the top3  
1191 intensity (not log transformed, unique for gene) of each kinase in proportion to the summed top3  
1192 intensity (not log transformed) of all AGC1 and AGC3 kinases (Fig. 2c). For clear visualization  
1193 only the D6PK family (D6PK, D6PKL1, D6PKL2, D6PKL3), AGC1.5, AGC1.6 and AGC1.7 were  
1194 colored in the plot.

1195 Mutant alleles of the *D6PK* family kinase genes, *d6pk-1*, *d6pk1-1*, *d6pk12-2* and *d6pk13-2*, and  
1196 their combinations were previously described <sup>111</sup>. Embryos were prepared omitting fixation with  
1197 ethanol/acetic acid as previously described <sup>112</sup>. Embryos were analyzed with a Zeiss Axio  
1198 Imager.M2, AxioCam 512 camera and 20x/0,8 Plan Apochromat objective using differential  
1199 interference contrast (DIC).

1200 For promoter:GUS constructs of *AGC1.5*, *AGC1.6* or *AGC1.7*, 2916 bp, 1207 bp, or 2214 bp  
1201 fragments upstream from the respective start codon were cloned into the *SalI* and *EcoRI* sites of  
1202 pCAMBIA1391Z. Flowers from transgenic plants, obtained by the floral-dip method<sup>50</sup>, were first  
1203 incubated in 90% cold acetone for 15 min followed by a  $\beta$ -glucuronidase (GUS)-staining solution  
1204 (50 mM sodium phosphate pH 7.0, 10 mM EDTA, 2 mM potassium ferricyanide, 2 mM  
1205 potassium ferrocyanide, 0.1% Triton-X100, 0.5 mg/ml 5-bromo-4-chloro-3-indolyl- $\beta$ -D-  
1206 glucuronide) over-night in the dark. Following a wash in 70% ethanol, flowers were incubated in  
1207 ethanol/acetate (6:1) for removing of chlorophyll and then rehydrated in a graded ethanol series  
1208 (90%, 70%, 50%, 30%). Samples were mounted in chloral hydrate/glycerol/water (8 g:1 ml: 2  
1209 ml) for imaging. The experiment was performed two times and GUS signal was observed for  
1210 12/18 *AGC1.5p::GUS*, 0/20 *AGC1.6p::GUS* and 12/18 *AGC1.7p::GUS* independent lines.

#### 1211 ***ABA response of RCAR phosphomutants***

1212 Preparation and analysis of Arabidopsis protoplasts was performed as described<sup>113</sup>. Briefly,  
1213 protoplasts from three weeks-old Col-0 plants ( $10^5$  protoplasts; 0.1 ml) were transfected with 5  
1214  $\mu$ g of reporter construct (*pRD29B::LUC*), 3  $\mu$ g of *p35S::GUS* plasmid as internal control and  
1215 3  $\mu$ g of effector plasmid. The effector plasmids drive expression of respective RCAR and PP2C  
1216 cDNAs under control of the 35S promoter<sup>114</sup>. RCAR10 phosphomimic reporter constructs  
1217 (RCAR10<sub>S32D</sub>; RCAR10<sub>S113D</sub>) were obtained by site-directed mutagenesis using primer pairs  
1218 S32D\_F/S32D\_R and S113D\_F/S113D\_R, respectively (Supplementary Data 11). The  
1219 protoplast suspension was incubated at various levels of ABA as indicated and reporter  
1220 expression was determined after 18 h of incubation at 25°C. Three biological replicates per data  
1221 point were performed for each assay. All data points were normalized to the empty vector  
1222 control. Structural modeling for RCAR10 was performed with SWISS-MODEL<sup>115</sup> using RCAR11  
1223 as template model (PDB ID 3k3k<sup>45,116</sup>) and modified with UCSF CHIMERA<sup>117</sup>.

#### 1224 ***Phenotypic characterization of QKY phosphomutants***

1225 The pCAMBIA2300-based pQKY::mCherry:QKY construct was described previously<sup>42</sup>. The  
1226 pQKY::mCherry:QKY<sub>S262A</sub> and pQKY::mCherry:QKY<sub>S262E</sub> plasmids were obtained using the Q5  
1227 site-directed mutagenesis kit (NEB, #E0554S) according to the manufacturers recommendation.  
1228 Primers are Q5SDM S262A\_F and Q5SDM S262A\_R for pQKY::mCherry:QKY<sub>S262A</sub> and  
1229 Q5SDM S262E\_F and Q5SDM S262E\_R for pQKY::mCherry:QKY<sub>S262E</sub> (Supplementary Data  
1230 11). All PCR-based constructs were confirmed by sequencing. Floral tissue for quantitative real-  
1231 time PCR (qPCR) was harvested from plants grown under long day conditions. With minor  
1232 changes, tissue collection, RNA extraction and qPCR analysis were performed as described

1233 <sup>118,119</sup>. For detection of *mCherry:QKY*, expression by qPCR, primers mCherry-qRT-For/mCherry-  
1234 qRT-Rev were employed (Table). Average *mCherry:QKY* expression was calculated relative to  
1235 the expression of three control genes (AT4G33380; AT2G28390; AT5G46630) (Supplementary  
1236 Data 11) and normalized to the wild type control for visualization. *A. thaliana* (L.) Heynh. var.  
1237 Landsberg (*erecta*) (Ler) was used as wild type strain. The likely null allele *qky-9* (Ler) has been  
1238 described previously <sup>43</sup>. *qky-9* mutant plants were transformed using Agrobacterium strain  
1239 GV3101/pMP90 <sup>120</sup> and the floral dip method <sup>50</sup>. Transgenic T1 plants were selected on  
1240 Kanamycin (50 µg/ml) and transferred to soil for further inspection. Plants were grown as  
1241 described earlier <sup>43</sup>. Four out of 17 independent T1 transformants showed a wild type phenotype  
1242 for the S262A transgenic line, while 13/17 T1 transformants displayed no (7/17) or partial (6/17)  
1243 rescue, a notable decrease in functionality compared to the wild type construct (14/17 rescue,  
1244 2/17 partial rescue, 1/17 no rescue). For the S262E transgene, 11 out of 13 independent T1  
1245 transformants showed a wild type phenotype (1/13 partial rescue, 1/13 no rescue).

1246 Floral organs were imaged using a Leica SAPO stereo microscope equipped with a digital MC  
1247 170 HD camera (Leica Microsystems GmbH, Wetzlar, Germany). Images were adjusted for  
1248 color and contrast using ImageJ/Fiji software <sup>121</sup>. Confocal laser scanning microscopy of *qky-9*  
1249 *pQKY::mCherry:QKY*, *qky-9 pQKY::mCherry:QKY<sub>S262A</sub>* and *qky-9 pQKY::mCherry:QKYS<sub>262E</sub>*  
1250 six days-old seedling roots was performed with an Olympus FV1000 setup using an inverted  
1251 IX81 stand and FluoView software (FV10-ASW version 01.04.00.09) (Olympus Europa GmbH,  
1252 Hamburg, Germany) equipped with a water-corrected 40x objective (NA 0.9) at 3x digital zoom.  
1253 Confocal high sensitivity detection (HSD) was employed involving two gallium arsenide  
1254 phosphide photomultipliers (GaAsP PMTs) mounted equidistantly to the probe. The experiment  
1255 was performed two times independently with 2 and 12 roots for *qky-9 pQKY::mCherry:QKY*, 6  
1256 and 15 roots for *qky-9 pQKY::mCherry:QKY<sub>S262A</sub>* and 15 roots for *qky-9*  
1257 *pQKY::mCherry:QKYS<sub>262E</sub>*.

## 1258 **Locus identifiers**

1259 Gene locus identifiers are listed for all gene names mentioned in the manuscript  
1260 (Supplementary Data 11).

## 1261 **Online methods references**

- 1262 44 Heazlewood, J. L., Verboom, R. E., Tonti-Filippini, J., Small, I. & Millar, A. H. SUBA: the  
1263 Arabidopsis Subcellular Database. *Nucleic Acids Res* **35**, D213-218, doi:10.1093/nar/gkl863  
1264 (2007).  
1265 45 Nishimura, N. *et al.* Structural mechanism of abscisic acid binding and signaling by dimeric PYR1.  
1266 *Science* **326**, 1373-1379, doi:10.1126/science.1181829 (2009).



1267 46 Smyth, D. R., Bowman, J. L. & Meyerowitz, E. M. Early flower development in Arabidopsis. *Plant*  
1268 *Cell* **2**, 755-767, doi:10.1105/tpc.2.8.755 (1990).

1269 47 Johnson-Brousseau, S. A. & McCormick, S. A compendium of methods useful for characterizing  
1270 Arabidopsis pollen mutants and gametophytically-expressed genes. *Plant J* **39**, 761-775,  
1271 doi:10.1111/j.1365-313X.2004.02147.x (2004).

1272 48 Sprunck, S. *et al.* Egg cell-secreted EC1 triggers sperm cell activation during double fertilization.  
1273 *Science* **338**, 1093-1097, doi:10.1126/science.1223944 (2012).

1274 49 Karimi, M., Inze, D. & Depicker, A. GATEWAY vectors for Agrobacterium-mediated plant  
1275 transformation. *Trends Plant Sci* **7**, 193-195 (2002).

1276 50 Clough, S. J. & Bent, A. F. Floral dip: a simplified method for Agrobacterium-mediated  
1277 transformation of Arabidopsis thaliana. *Plant J* **16**, 735-743 (1998).

1278 51 Schmid, M. *et al.* A gene expression map of Arabidopsis thaliana development. *Nat Genet* **37**,  
1279 501-506, doi:10.1038/ng1543 (2005).

1280 52 Boyes, D. C. *et al.* Growth stage-based phenotypic analysis of Arabidopsis: a model for high  
1281 throughput functional genomics in plants. *Plant Cell* **13**, 1499-1510 (2001).

1282 53 Bowman, J. L. *Arabidopsis : an atlas of morphology and development.* (Springer-Verlag, 1994).

1283 54 Bradford, M. M. A rapid and sensitive method for the quantitation of microgram quantities of  
1284 protein utilizing the principle of protein-dye binding. *Anal Biochem* **72**, 248-254 (1976).

1285 55 Ruprecht, B. *et al.* Optimized Enrichment of Phosphoproteomes by Fe-IMAC Column  
1286 Chromatography. *Methods Mol Biol* **1550**, 47-60, doi:10.1007/978-1-4939-6747-6\_5 (2017).

1287 56 Marx, H. *et al.* A large synthetic peptide and phosphopeptide reference library for mass  
1288 spectrometry-based proteomics. *Nat Biotechnol* **31**, 557-564, doi:10.1038/nbt.2585 (2013).

1289 57 Ruprecht, B., Zecha, J., Zolg, D. P. & Kuster, B. High pH Reversed-Phase Micro-Columns for  
1290 Simple, Sensitive, and Efficient Fractionation of Proteome and (TMT labeled) Phosphoproteome  
1291 Digests. *Methods Mol Biol* **1550**, 83-98, doi:10.1007/978-1-4939-6747-6\_8 (2017).

1292 58 Smith, P. K. *et al.* Measurement of protein using bicinchoninic acid. *Anal Biochem* **150**, 76-85,  
1293 doi:10.1016/0003-2697(85)90442-7 (1985).

1294 59 Zolg, D. P. *et al.* PROCAL: A Set of 40 Peptide Standards for Retention Time Indexing, Column  
1295 Performance Monitoring, and Collision Energy Calibration. *Proteomics* **17**,  
1296 doi:10.1002/pmic.201700263 (2017).

1297 60 Hahne, H. *et al.* DMSO enhances electrospray response, boosting sensitivity of proteomic  
1298 experiments. *Nat Methods* **10**, 989-991, doi:10.1038/nmeth.2610 (2013).

1299 61 Bian, Y. *et al.* Robust, reproducible and quantitative analysis of thousands of proteomes by  
1300 micro-flow LC-MS/MS. *Nat Commun* **11**, 157, doi:10.1038/s41467-019-13973-x (2020).

1301 62 Tyanova, S., Temu, T. & Cox, J. The MaxQuant computational platform for mass spectrometry-  
1302 based shotgun proteomics. *Nat Protoc* **11**, 2301-2319, doi:10.1038/nprot.2016.136 (2016).

1303 63 Hanada, K. *et al.* sORF finder: a program package to identify small open reading frames with high  
1304 coding potential. *Bioinformatics* **26**, 399-400, doi:10.1093/bioinformatics/btp688 (2010).

1305 64 Grabherr, M. G. *et al.* Full-length transcriptome assembly from RNA-Seq data without a  
1306 reference genome. *Nat Biotechnol* **29**, 644-652, doi:10.1038/nbt.1883 (2011).

1307 65 Li, W., Jaroszewski, L. & Godzik, A. Clustering of highly homologous sequences to reduce the size  
1308 of large protein databases. *Bioinformatics* **17**, 282-283, doi:10.1093/bioinformatics/17.3.282  
1309 (2001).

1310 66 Perkins, D. N., Pappin, D. J., Creasy, D. M. & Cottrell, J. S. Probability-based protein identification  
1311 by searching sequence databases using mass spectrometry data. *Electrophoresis* **20**, 3551-3567,  
1312 doi:10.1002/(SICI)1522-2683(19991201)20:18<3551::AID-ELPS3551>3.0.CO;2-2 (1999).

1313 67 Franken, H. *et al.* Thermal proteome profiling for unbiased identification of direct and indirect  
1314 drug targets using multiplexed quantitative mass spectrometry. *Nat Protoc* **10**, 1567-1593,  
1315 doi:10.1038/nprot.2015.101 (2015).

1316 68 Toprak, U. H. *et al.* Conserved peptide fragmentation as a benchmarking tool for mass  
1317 spectrometers and a discriminating feature for targeted proteomics. *Mol Cell Proteomics* **13**,  
1318 2056-2071, doi:10.1074/mcp.O113.036475 (2014).

1319 69 Onate-Sanchez, L. & Vicente-Carbajosa, J. DNA-free RNA isolation protocols for Arabidopsis  
1320 thaliana, including seeds and siliques. *BMC Res Notes* **1**, 93, doi:10.1186/1756-0500-1-93 (2008).

1321 70 Bolger, A. M., Lohse, M. & Usadel, B. Trimmomatic: a flexible trimmer for Illumina sequence  
1322 data. *Bioinformatics* **30**, 2114-2120, doi:10.1093/bioinformatics/btu170 (2014).

1323 71 Bray, N. L., Pimentel, H., Melsted, P. & Pachter, L. Near-optimal probabilistic RNA-seq  
1324 quantification. *Nat Biotechnol* **34**, 525-527, doi:10.1038/nbt.3519 (2016).

1325 72 Silva, J. C., Gorenstein, M. V., Li, G. Z., Vissers, J. P. & Geromanos, S. J. Absolute quantification of  
1326 proteins by LCMSE: a virtue of parallel MS acquisition. *Mol Cell Proteomics* **5**, 144-156,  
1327 doi:10.1074/mcp.M500230-MCP200 (2006).

1328 73 The Gene Ontology, C. Expansion of the Gene Ontology knowledgebase and resources. *Nucleic  
1329 Acids Res* **45**, D331-D338, doi:10.1093/nar/gkw1108 (2017).

1330 74 Cox, J. & Mann, M. 1D and 2D annotation enrichment: a statistical method integrating  
1331 quantitative proteomics with complementary high-throughput data. *BMC Bioinformatics* **13  
1332 Suppl 16**, S12, doi:10.1186/1471-2105-13-S16-S12 (2012).

1333 75 Tyanova, S. *et al.* The Perseus computational platform for comprehensive analysis of  
1334 (prote)omics data. *Nat Methods* **13**, 731-740, doi:10.1038/nmeth.3901 (2016).

1335 76 Olsen, J. V. *et al.* Global, in vivo, and site-specific phosphorylation dynamics in signaling  
1336 networks. *Cell* **127**, 635-648, doi:10.1016/j.cell.2006.09.026 (2006).

1337 77 Uhlen, M. *et al.* Transcriptomics resources of human tissues and organs. *Mol Syst Biol* **12**, 862,  
1338 doi:10.15252/msb.20155865 (2016).

1339 78 Rijpkema, A. S., Vandenbussche, M., Koes, R., Heijmans, K. & Gerats, T. Variations on a theme:  
1340 changes in the floral ABCs in angiosperms. *Semin Cell Dev Biol* **21**, 100-107,  
1341 doi:10.1016/j.semcdb.2009.11.002 (2010).

1342 79 Loytynoja, A. Phylogeny-aware alignment with PRANK. *Methods Mol Biol* **1079**, 155-170,  
1343 doi:10.1007/978-1-62703-646-7\_10 (2014).

1344 80 Castresana, J. Selection of conserved blocks from multiple alignments for their use in  
1345 phylogenetic analysis. *Mol Biol Evol* **17**, 540-552, doi:10.1093/oxfordjournals.molbev.a026334  
1346 (2000).

1347 81 Yang, Z. PAML 4: phylogenetic analysis by maximum likelihood. *Mol Biol Evol* **24**, 1586-1591,  
1348 doi:10.1093/molbev/msm088 (2007).

1349 82 van der Graaf, A. *et al.* Rate, spectrum, and evolutionary dynamics of spontaneous  
1350 epimutations. *Proc Natl Acad Sci U S A* **112**, 6676-6681, doi:10.1073/pnas.1424254112 (2015).

1351 83 Gebert, D., Jehn, J. & Rosenkranz, D. Widespread selection for extremely high and low levels of  
1352 secondary structure in coding sequences across all domains of life. *Open Biol* **9**, 190020,  
1353 doi:10.1098/rsob.190020 (2019).

1354 84 Camiolo, S., Melito, S. & Porceddu, A. New insights into the interplay between codon bias  
1355 determinants in plants. *DNA Res* **22**, 461-470, doi:10.1093/dnares/dsv027 (2015).

1356 85 Drummond, D. A., Bloom, J. D., Adami, C., Wilke, C. O. & Arnold, F. H. Why highly expressed  
1357 proteins evolve slowly. *Proc Natl Acad Sci U S A* **102**, 14338-14343,  
1358 doi:10.1073/pnas.0504070102 (2005).

1359 86 Das, S. & Bansal, M. Variation of gene expression in plants is influenced by gene architecture  
1360 and structural properties of promoters. *PLoS One* **14**, e0212678,  
1361 doi:10.1371/journal.pone.0212678 (2019).

1362 87 Celaj, A. *et al.* Quantitative analysis of protein interaction network dynamics in yeast. *Mol Syst*  
1363 *Biol* **13**, 934, doi:10.15252/msb.20177532 (2017).

1364 88 Niederhuth, C. E. *et al.* Widespread natural variation of DNA methylation within angiosperms.  
1365 *Genome Biol* **17**, 194, doi:10.1186/s13059-016-1059-0 (2016).

1366 89 Love, M. I., Huber, W. & Anders, S. Moderated estimation of fold change and dispersion for  
1367 RNA-seq data with DESeq2. *Genome Biol* **15**, 550, doi:10.1186/s13059-014-0550-8 (2014).

1368 90 Zhou, X. & Stephens, M. Genome-wide efficient mixed-model analysis for association studies.  
1369 *Nat Genet* **44**, 821-824, doi:10.1038/ng.2310 (2012).

1370 91 Nakazawa, N. fmsb: Functions for Medical Statistics Book with some Demographic Data. R  
1371 package version 0.6.3. <https://CRAN.R-project.org/package=fmsb> (2018).

1372 92 R Core Team. R: A language and environment for statistical computing. *R Foundation for*  
1373 *Statistical Computing* (<https://www.R-project.org/>) (2014).

1374 93 Tibshirani, R. Regression Shrinkage and Selection via the Lasso. *Journal of the Royal Statistical*  
1375 *Society* **58**, 267-288 (1996).

1376 94 Zhang, Z. Variable selection with stepwise and best subset approaches. *Ann Transl Med* **4**, 136,  
1377 doi:10.21037/atm.2016.03.35 (2016).

1378 95 Knecht, W. Pilot Willingness to take Off Into Marginal Weather, Part II: Antecedent Overfitting  
1379 With Forward Stepwise Logistic Regression. *Final Report, Federal Aviation Administration* (2005).

1380 96 Friedman, J., Hastie, T. & Tibshirani, R. Regularization Paths for Generalized Linear Models via  
1381 Coordinate Descent. *J Stat Softw* **33**, 1-22 (2010).

1382 97 Groemping, U. Relative importance for linear regression in R: The package relaimpo. *Journal of*  
1383 *Statistical Software* **17**, 1-27, doi: 10.18637/jss.v017.i01 (2007).

1384 98 Heusel, M. *et al.* Complex-centric proteome profiling by SEC-SWATH-MS. *Mol Syst Biol* **15**,  
1385 e8438, doi:10.15252/msb.20188438 (2019).

1386 99 McBride, Z., Chen, D., Reick, C., Xie, J. & Szymanski, D. B. Global Analysis of Membrane-  
1387 associated Protein Oligomerization Using Protein Correlation Profiling. *Mol Cell Proteomics* **16**,  
1388 1972-1989, doi:10.1074/mcp.RA117.000276 (2017).

1389 100 Ruepp, A. *et al.* CORUM: the comprehensive resource of mammalian protein complexes--2009.  
1390 *Nucleic Acids Res* **38**, D497-501, doi:10.1093/nar/gkp914 (2010).

1391 101 Zhang, B. & Horvath, S. A general framework for weighted gene co-expression network analysis.  
1392 *Stat Appl Genet Mol Biol* **4**, Article17, doi:10.2202/1544-6115.1128 (2005).

1393 102 Langfelder, P., Zhang, B. & Horvath, S. Defining clusters from a hierarchical cluster tree: the  
1394 Dynamic Tree Cut package for R. *Bioinformatics* **24**, 719-720,  
1395 doi:10.1093/bioinformatics/btm563 (2008).

1396 103 Kanehisa, M., Furumichi, M., Tanabe, M., Sato, Y. & Morishima, K. KEGG: new perspectives on  
1397 genomes, pathways, diseases and drugs. *Nucleic Acids Res* **45**, D353-D361,  
1398 doi:10.1093/nar/gkw1092 (2017).

1399 104 Fabregat, A. *et al.* The Reactome pathway Knowledgebase. *Nucleic Acids Res* **44**, D481-487,  
1400 doi:10.1093/nar/gkv1351 (2016).

1401 105 Hochberg, Y. B. a. Y. Controlling the false discovery rate: a practical and powerful approach to  
1402 multiple testing. *Journal of the Royal Statistical Society* **57**, 289-300 (1995).

1403 106 Subramanian, A. *et al.* Gene set enrichment analysis: a knowledge-based approach for  
1404 interpreting genome-wide expression profiles. *Proc Natl Acad Sci U S A* **102**, 15545-15550,  
1405 doi:10.1073/pnas.0506580102 (2005).

1406 107 List, M. *et al.* KeyPathwayMinerWeb: online multi-omics network enrichment. *Nucleic Acids Res*  
1407 **44**, W98-W104, doi:10.1093/nar/gkw373 (2016).

1408 108 Letunic, I. & Bork, P. 20 years of the SMART protein domain annotation resource. *Nucleic Acids*  
1409 *Res* **46**, D493-D496, doi:10.1093/nar/gkx922 (2018).

1410 109 Wagih, O. ggseqlogo: a versatile R package for drawing sequence logos. *Bioinformatics* **33**, 3645-  
1411 3647, doi:10.1093/bioinformatics/btx469 (2017).

1412 110 Goel, R., Harsha, H. C., Pandey, A. & Prasad, T. S. Human Protein Reference Database and  
1413 Human Proteinpedia as resources for phosphoproteome analysis. *Mol Biosyst* **8**, 453-463,  
1414 doi:10.1039/c1mb05340j (2012).

1415 111 Zourelidou, M. *et al.* The polarly localized D6 PROTEIN KINASE is required for efficient auxin  
1416 transport in *Arabidopsis thaliana*. *Development* **136**, 627-636, doi:10.1242/dev.028365 (2009).

1417 112 Mayer, U. B., G.; Jurgens, G. Apical-basal pattern formation in the *Arabidopsis* embryo: studies  
1418 on the role of the *gnom* gene. *Development* **177**, 149-162 (1993).

1419 113 Moes, D., Himmelbach, A., Korte, A., Haberer, G. & Grill, E. Nuclear localization of the mutant  
1420 protein phosphatase *abi1* is required for insensitivity towards ABA responses in *Arabidopsis*.  
1421 *Plant J* **54**, 806-819, doi:10.1111/j.1365-313X.2008.03454.x (2008).

1422 114 Tischer, S. V. *et al.* Combinatorial interaction network of abscisic acid receptors and coreceptors  
1423 from *Arabidopsis thaliana*. *Proc Natl Acad Sci U S A* **114**, 10280-10285,  
1424 doi:10.1073/pnas.1706593114 (2017).

1425 115 Waterhouse, A. *et al.* SWISS-MODEL: homology modelling of protein structures and complexes.  
1426 *Nucleic Acids Res* **46**, W296-W303, doi:10.1093/nar/gky427 (2018).

1427 116 Berman, H. M. *et al.* The Protein Data Bank. *Nucleic Acids Res* **28**, 235-242 (2000).

1428 117 Pettersen, E. F. *et al.* UCSF Chimera--a visualization system for exploratory research and analysis.  
1429 *J Comput Chem* **25**, 1605-1612, doi:10.1002/jcc.20084 (2004).

1430 118 Box, M. S., Coustham, V., Dean, C. & Mylne, J. S. Protocol: A simple phenol-based method for 96-  
1431 well extraction of high quality RNA from *Arabidopsis*. *Plant Methods* **7**, 7, doi:10.1186/1746-  
1432 4811-7-7 (2011).

1433 119 Enugutti, B. *et al.* Regulation of planar growth by the *Arabidopsis* AGC protein kinase UNICORN.  
1434 *Proc Natl Acad Sci U S A* **109**, 15060-15065, doi:10.1073/pnas.1205089109 (2012).

1435 120 Koncz, C. & Schell, J. The promoter of TL-DNA gene 5 controls the tissue-specific expression of  
1436 chimaeric genes carried by a novel type of *Agrobacterium* binary vector. *Molecular and General*  
1437 *Genetics MGG* **204**, 383-396, doi:10.1007/bf00331014 (1986).

1438 121 Schindelin, J. *et al.* Fiji: an open-source platform for biological-image analysis. *Nat Methods* **9**,  
1439 676-682, doi:10.1038/nmeth.2019 (2012).

1440 122 Vizcaino, J. A. *et al.* 2016 update of the PRIDE database and its related tools. *Nucleic Acids Res*  
1441 **44**, D447-456, doi:10.1093/nar/gkv1145 (2016).

1442

1443 **Acknowledgements**

1444 We thank the NGS@tum core facility for RNA sequencing, Rachele Tofanelli for help with  
1445 imaging the ovules, Robert J. Schmitz for providing data access for the feature analysis and  
1446 Maria Reinecke, Florian Bayer and Stefanie Galinec for MS measurements. This work was in  
1447 part funded by the German Science Foundation (DFG, SFB924), a research fellowship to HS by  
1448 the Japan Society for the Promotion of Sciences and a research fellowship to XC by the  
1449 Chinese Research Council.

1450 **Author contributions**

1451 JM performed (phosho)proteomic and transcriptomic experiments under the supervision of BK.  
1452 SR and HS performed AGC kinase experiments in plants under the supervision of GJ and CS.  
1453 MP, AC and XC performed phosphomutant analysis under the supervision of EG and KS. PC  
1454 and SS generated and provided plant material. JM, MF, MM, DL, SA, DPZ, TM, CD, AD and  
1455 RRH performed data analysis under the supervision of BK, KFXM, PF, MB, TH and FJ. ML, PS  
1456 and TS generated Arabidopsis resource databases under supervision of MW and JB. JM, CS  
1457 and BK conceptualized the project and wrote the manuscript. All authors edited the manuscript.

1458 **Competing interests**

1459 MW and BK are founders and shareholders of OmicScouts GmbH and msAId GmbH. They  
1460 have no operational role in the companies. MF and DPZ are founders and shareholders of  
1461 msAId GmbH. TM and MB are employees and/or shareholders of Cellzome GmbH. The  
1462 remaining authors declare no competing interests.

1463 **Data and software availability**

1464 The data supporting the findings of this study are available within the paper, the supplementary  
1465 information and the public repositories. Source data for main Figure 1-5 and Extended Data  
1466 Figure 1-9 are included. Transcriptome sequencing and quantification data are available at  
1467 ArrayExpress ([www.ebi.ac.uk/arrayexpress](http://www.ebi.ac.uk/arrayexpress)) under the identifier E-MTAB-7978. The raw mass  
1468 spectrometric data and MaxQuant result files have been deposited to the ProteomeXchange  
1469 Consortium via PRIDE <sup>122</sup>, with the dataset identifier PXD013868.

1470 **Corresponding author:** Bernhard Kuster ([kuster@tum.de](mailto:kuster@tum.de))

1471

1472 **Extended data figure legends**

1473 **Extended Data Figure 1 | Descriptive analysis of the multi-omic tissue atlas.**

1474 a, Pairwise global Pearson expression correlation analysis of all 30 tissues (n = 1 measurement  
1475 per tissue) on the transcriptome level (lower triangle) and proteome level (upper triangle) using  
1476 all identified gene loci. The data shows that proteins correlate more strongly between tissues  
1477 than transcripts. Turquoise squares mark examples for morphologically highly similar tissues.  
1478 Tissues are coloured as in Figure 1: Flower (light grey), seed (dark brown), pollen (yellow), stem  
1479 (dark green), leaf (light green), root (dark grey), fruit (light brown), callus (magenta), cell culture  
1480 (blue).

1481 b, Scatter plots showing highly reproducible abundance measurements for transcript (upper  
1482 panels) and protein (lower panels) in morphologically similar tissues that were marked in panel  
1483 a, namely node (ND) versus internode (IND), leaf distal (LFD) versus leaf proximal (LFP) and  
1484 root (RT) versus root upper zone (RTUZ). *R* denotes the Pearson correlation coefficient and *n*  
1485 denotes the number of transcripts or proteins shown in the plots.

1486 c, Percentage of genes encoded by a specific chromosome that were identified at the  
1487 transcriptome, proteome or phosphoproteome level.

1488 d, Percentage of Swiss-Prot and TrEMBL protein database entries as well as protein evidence  
1489 categories from UniProt that were identified at the transcriptome, proteome or  
1490 phosphoproteome level. Evidence level: (1) 'protein evidence', (2) 'transcript evidence', (3)  
1491 'homology', (4) 'predicted', (5) 'uncertain'.

1492 e, Comparison of protein identifications between an earlier Arabidopsis proteome study by  
1493 Baerenfaller et al. based on 12 tissues <sup>7</sup>, this study (30 tissues) and the number of protein-  
1494 coding genes in Araport11.

1495 f, iBAQ intensity distribution of proteins identified in this study. Proteins also identified by  
1496 Baerenfaller et al. are projected into the same plot.

1497 g, Left panel: Proportion of identified p-sites on S, T or Y residues with highly confident  
1498 localization of the phosphorylation site within the identified peptide sequence (termed class I p-  
1499 sites if the localization score is >0.75). Right panel: distribution of proteins for which  
1500 phosphorylated S, T or Y residues were identified.

1501 h, Left panel: Venn diagram comparing phosphoprotein datasets from van Wijk et al. <sup>8</sup>,  
1502 PhosPhAT4.0 and this study. Right panel: Venn diagram comparing p-site localization  
1503 confidence between class I sites identified in this study and the low and high confidence  
1504 datasets reported by van Wijk et al.

1505 **Extended Data Figure 2 | Proteogenomics and dynamic range of transcript and protein**  
1506 **expression.**

1507 a, Number of identified N-terminal (NT) or C-terminal (CT) peptides of proteins in either  
1508 unmodified or phosphorylated form.

1509 b, Frequency of amino acids following the initiator methionine in N-terminal peptides with (-X) or  
1510 without cleavage of the initiator methionine (M-X). X denotes the amino acid following the start  
1511 codon.

1512 c, Frequency of protein N-terminal acetylation for amino acids in (b). Because trypsin was used  
1513 for protein digestion, the frequencies for arginine (R) and lysine (K) could not be determined  
1514 (n.d.).

1515 d, Distribution of peptide-based sequence coverage of proteins in individual tissues and for the  
1516 combined dataset (tissue abbreviations as in Figure 1). Boxes contain 50% of the data and  
1517 show the median as a black line. The upper and lower quartile ranges are shown as whiskers.  
1518 The number of proteins is indicated for each tissue.

1519 e, Pie charts showing the percentage of proteins identified by <3, 3-10 or >10 peptides either  
1520 allowing shared (razor) peptides or restricting to unique peptides only.

1521 f, Left panel: number of protein isoforms detected at the transcript and protein level compared to  
1522 the number of all annotated isoforms in Araport11. Right panel: Number of multiple isoforms of  
1523 the same gene distinguished at the peptide level.

1524 g, Validation of protein isoform and short open reading frame (sORF) identification by  
1525 comparing the tandem mass spectra from the tissue atlas to those of synthetic peptide  
1526 reference standards. The normalized spectral contrast angle (SA) was used as a similarity  
1527 metric (see methods). Candidate isoforms and sORFs were considered valid if the SA of the  
1528 spectra was >0.7. This data is reported in Supplementary Data 3.

1529 h, Amino acid sequence and mirror plots of tandem mass spectra for two peptides of the sORF  
1530 BIP138\_4. The spectra pointing upwards were collected from tissue digests, those pointing  
1531 downwards were collected from synthetic peptides. The normalized spectral contrast angle (SA)  
1532 and Pearson correlation coefficient (*R*) were used as similarity metrics (see methods) and  
1533 indicate that both high scoring spectra (n=1 acquired spectra) are near identical, thus validating  
1534 the identification of this sORF as a expressed protein.

1535 i, Dynamic range of transcript expression (grey) and proportion of transcripts that were also  
1536 identified at the protein level projected into this plot (blue). OM: orders of magnitude. Note that  
1537 for lower abundance transcripts, fewer proteins were detected.

1538 j, Dynamic range of protein expression and proportion of proteins with phosphorylation  
1539 evidence. Note that protein expression spans 6 OM whereas transcript expression only spans 4  
1540 OM (panel i). Further note that phosphorylation was detected across the entire protein  
1541 expression range.

1542 k, Percentage of all annotated kinases (K), phosphatases (P), transcription factors (TF) and  
1543 transcription regulators (TR) detected at the transcript, protein or phosphoprotein level.  
1544 Numbers below the x-axis denote the number of genes for these protein classes in the AT  
1545 genome.

1546 **Extended Data Figure 3 | Descriptive analysis of transcript and protein expression in**  
1547 **tissues.**

1548 a. Distribution of expression specificity categories for protein and transcript identifications. See  
1549 online methods for the definition of these categories. Briefly, there are very few transcripts and  
1550 proteins that are only expressed in a single tissue. Note that the quantities of the shared  
1551 transcripts or proteins can differ vastly between tissues (see below).

1552 b, Left panel: protein identifications shared between flower (FL) and flower organs showing an  
1553 almost complete qualitative overlap of proteins. Sepal (SP), petal (PT), stamen (ST), carpel  
1554 (CP). Right panel: clustering of z-scored protein intensities showing distinct quantitative  
1555 expression differences between flower organs.

1556 c, Expression analysis of flower organ identity marker at the protein and transcript level.  
1557 PISTILLATA (PI, green), APETALA3 (AP3, red), APETALA1 (AP1, orange), AGAMOUS (AG,  
1558 blue). The expression of these markers is in line with the model of flower organ identity (AP1  
1559 expression marking sepal, AP1, AP3, PI marking petal, AG, AP3, PI marking stamen and AG  
1560 marking carpel).

1561 d, Total number of transcripts plotted against the total number of proteins detected in each  
1562 individual tissue ( $n = 30$  tissues) showing that the more genes are expressed as mRNAs, the  
1563 more proteins can be detected in a tissue (Pearson correlation  $R = 0.79$ ). Tissues are coloured  
1564 according to tissue groups as in Figure 1.

1565 e, Cumulative abundance plots of intensity-ranked identifications of transcripts and proteins for  
1566 five representative tissues. The five most abundant transcripts and proteins are listed in  
1567 descending order for each tissue. Note that these are generally not the same. Further note that  
1568 the characteristics of the plots are not the same for all tissues. In flower, the protein line rises  
1569 more quickly than the transcript line. The opposite is true for pollen and a more even  
1570 characteristic is observed in seed.

1571 f, Distribution of shared and unique identifications among the 100 most abundant transcripts and  
1572 proteins in each tissue. Note that relatively few proteins and transcripts are found together on



1573 the list of the 100 most abundant transcripts and proteins. This demonstrates that the  
1574 quantitative differences in transcript and protein expression are more important in defining a  
1575 tissue than the qualitative expression of transcripts or proteins.

1576 g, List of 11 proteins which were found as the most abundant protein (in at least one tissue) and  
1577 their proportion of the total iBAQ intensity in each tissue. Note that individual proteins can  
1578 represent up to 9% of the total protein in a given tissue.

1579 h, Principal component analysis (PCA) of the core tissue proteomes and transcriptomes (i.e. the  
1580 proteins and transcripts that were identified in every tissue) using z-scored abundances. Note  
1581 that only about 30% of all protein and 20% of all mRNAs were detected in every of the 30  
1582 tissues despite the fact that all tissues were deeply profiled at both protein and transcript level.  
1583 This shows that strong qualitative and quantitative expression differences exist between tissues.  
1584 The PCA separates tissues into photosynthetically active versus inactive tissues (component 1)  
1585 and separates pollen from all other tissues (component 2) implying that the molecular  
1586 composition of pollen is particularly different from all other tissues.

1587 i, Proportion of the total summed protein intensity for genes with specific subcellular  
1588 compartment annotation (from SUBA <sup>44</sup>, see methods) in the different tissue groups. The  
1589 comparison of photosynthetically active and inactive tissues shows that e. g. a majority of the  
1590 protein content in photosynthetically active tissues are contained in the plastids, whereas most  
1591 protein is found in the cytosol for photosynthetically inactive tissues. Proteins with only one  
1592 single subcellular compartment annotation were selected for the plot and the proportion of their  
1593 iBAQ intensities were averaged for each tissue group. Nucleus (n = 1,393), endoplasmatic  
1594 reticulum (n = 58), golgi (n = 68), peroxisome (n = 67), plastid (n = 525), mitochondrion (n =  
1595 317), vacuole (n = 71), cytosol (n = 385), cytoskeleton (n = 1), plasma membrane (n = 268),  
1596 extracellular (n = 351).

1597 **Extended Data Figure 4 | Relationships between transcript and protein levels.**

1598 a, Pearson correlation ( $R$ ) of transcriptome and proteome expression (core datasets; n = 5,043)  
1599 for each tissue.

1600 b, Pearson correlation ( $R$ ) between measured and predicted protein abundance levels in all  
1601 tissues. Predicted protein abundance levels were obtained from the best fitting feature selection  
1602 model for each tissue (see methods). The number of genes used for the correlation analysis is  
1603 indicated for each tissue.

1604 c, Violin plots showing the spread in relative contribution of selected features to the prediction of  
1605 gene-level protein abundance across tissues (n = 30 tissues) using our model. Violin shapes  
1606 show the kernel density estimation of the data distribution and the median as white dot. Thick  
1607 black bars denote the interquartile range.

1608 d, Specific nucleotide sequence motifs in 5'UTRs of mRNAs contribute to the prediction of  
1609 protein levels in a subset of tissues. Clustering tissues based on the presence or absence of  
1610 detected 5'UTR motifs shows that several features are repeatedly selected for inclusion in the  
1611 model while others appear to be more tissue-specific.

1612 e, Based on the observation that the ratio of non-synonymous to synonymous nucleotide  
1613 substitutions (Dn/Ds) between orthologous of *Arabidopsis thaliana* and *Arabidopsis lyrata*  
1614 contributed to the prediction of protein levels (see above), we analysed this feature in more  
1615 detail. Left panel: Distribution of the ratio of non-synonymous to synonymous nucleotide  
1616 substitutions (Dn/Ds) for orthologous genes in *Arabidopsis thaliana* and *Arabidopsis lyrata*. The  
1617 distribution is plotted for the example of 'leaf distal' (n = 6,447 genes). To compare evolutionarily  
1618 conserved genes (defined by low non-synonymous to synonymous substitutions [Dn/Ds] ratios)  
1619 and genes that evolve neutrally or are under positive selection (high Dn/Ds), we selected the  
1620 bottom 5% and top 5% of the Dn/Ds ratio distribution, respectively. Right panel: evolutionarily  
1621 conserved genes (low Dn/Ds ratio) show 10-20x higher protein abundance than genes under  
1622 evolutionary pressure. Boxes contain 50% of the data and show the median as a black line.  
1623 Whiskers denote 1.5 times the interquartile range. Outliers were omitted from the plot for clarity.

1624 f, Time course analysis of median protein abundance changes upon cycloheximide (translation  
1625 block, CHX) or MG132 (proteasome block) treatment vs time-matched DMSO control samples  
1626 (see methods). Boxes contain 50% of the data and show medians as black lines. Whiskers  
1627 denote 1.5 times the interquartile range. Outliers were omitted from the plot for clarity but were  
1628 included in the statistical tests below. Shown are either all proteins in the experiment (n = 8,920,  
1629 grey), proteins that have a high (n = 425, red) or low (n = 254, blue) PTR in seed (defined as in  
1630 main Figure 3d). Differences between time points were tested for significance within each  
1631 subset (all; high PTR; low PTR) using one-way ANOVA (analysis of variance) and the post-hoc  
1632 Tukey HSD (Honestly significant difference) test. \*\*\* HSD p-Value < 0.001 (all\_CHX8-CHX16:  
1633 p-Value < 1e-7; all\_CHX8-CHX24: p-Value < 1e-7; all\_CHX16-CHX24: p-Value = 0.0002;  
1634 highPTR\_CHX8-CHX24: p-Value = 0.0003; lowPTR\_CHX8-CHX16: p-Value = 0.0000004;  
1635 lowPTR\_CHX8-CHX24: p-Value < 1e-7; lowPTR\_CHX16-CHX24: p-Value < 1e-7).

1636 g, Representative images of seeds after 4 days of incubation with CHX, MG132 or DMSO  
1637 control medium (n = 1). Germination was completely inhibited by CHX and partially inhibited by  
1638 MG132 showing that the drug treatments were effective.

1639 **Extended Data Figure 5 | Correlations between transcriptomes, proteomes and**  
1640 **phosphoproteomes.**

1641 a, Median protein to mRNA ratios (PTRs) across tissues plotted against the inter-tissue  
1642 variation of these PTRs (expressed as median absolute deviation, MAD; proteins and  
1643 transcripts had to be detected in at least 10 matching tissues to be included in the analysis).

1644 Examples for genes with low transcript/high protein (rbcL and petA), and high transcript/low  
1645 protein (IAA8 and IAA13) are marked by arrows. The bar blot shows the MAD range segmented  
1646 into 5 quantiles each containing the same number of genes (coloured bars and dashed lines). It  
1647 is evident that most genes have reasonably stable PTRs across tissues.

1648 b, Same as panel a (dataset  $n = 14,069$ ) but for transcript (left plot) and protein measurements  
1649 (right plot). As can be seen, there is somewhat more variation in protein levels across tissues  
1650 than there is mRNA variation (80% of all transcripts show a MAD of  $<1$ ; 80% of all proteins  
1651 show a MAD of 1.2). There is also more variation in the protein levels across tissues for low  
1652 abundant proteins. This may in part due to technical limitations as low abundance proteins can  
1653 generally be less accurately quantified.

1654 c, Same as panel a but for the ratio of phosphorylation site versus protein abundance. P-sites  
1655 and proteins had to be detected in at least 10 matching tissues to be included in the analysis  
1656 ( $n = 13,793$ ).

1657 d, Same as panel b (dataset  $n = 13,793$ ) but for phosphorylation site abundance. Note that p-  
1658 site abundance shows somewhat greater variation across tissues than protein abundance (60%  
1659 of all p-sites show  $MAD < 1$  compared to 80% of all proteins, see panel b). Again, this may in part  
1660 due to technical limitations as p-site quantification is performed on a peptide level and does not  
1661 benefit from aggregating multiple peptide quantifications into one value for protein quantification.

1662 **Extended Data Figure 6 | Inferring redundant gene function and physical interactions**  
1663 **from co-expression analysis.**

1664 a, Scatter plot of Pearson correlation coefficients ( $R$ ) as a measure for co-expression across  
1665 tissues for all pairs of proteins (x-axis) and all pairs of transcripts (y-axis) (core dataset only,  $n =$   
1666  $5,043$ ) along with their marginal histograms. Colours denote the  $\log_2$ -normalized STRING  
1667 scores of individual gene pairs as a measure of known or predicted direct (physical) or indirect  
1668 (functional) associations. The data show that strong co-expression of transcripts or proteins or  
1669 both are more strongly related (physically or functionally) than transcripts and proteins that are  
1670 not.

1671 b, Co-expression analysis of duplicated genes (pairs had to be detected in at least 10 matching  
1672 tissues to be included in the analysis). The density plots show the distribution of Pearson  
1673 correlation coefficients ( $R$ ) of co-expressed transcripts (grey) or proteins (blue) for genes that  
1674 arose by whole genome duplications (WGD), local duplications (local) or transposon-mediated  
1675 duplications (transposed). Randomly selected gene pairs are shown as control (random).  
1676 Medians ( $\bar{x}$ ) are given and displayed as dotted lines. The data shows that there is substantial  
1677 co-expression of duplicated genes implying that these genes likely have redundant functions.

1678 c, Left panel: Protein level Pearson correlation coefficient ( $R$ ) values (from panel b) for all  
1679 duplicate gene pairs (WGD, local, transposed) plotted against the protein abundance ratio of  
1680 each pair (average across 30 tissues, see methods). Blue arrows point out one example each  
1681 for a high or low ratio of protein expression for the duplicated genes. Right panel: Example for  
1682 tissue-resolved protein intensity proportions (top3, see methods) for the duplicate pair: MAC5A  
1683 and MAC5B. The data shows that irrespective of the tissue, MAC5A is always much higher  
1684 expressed than MAC5B. Tissues are coloured as in Figure 1.

1685 d, Upper panel: ranked protein abundance ratio for selected duplicate pairs (average  $\pm$  SD;  $n =$   
1686 30) and annotated for phenotypic effects (lower panel) in the loss-of-function mutant for either  
1687 duplicate 1 or duplicate 2 (+). Absence of a phenotypic effect is marked by (-). The data shows  
1688 that asymmetric protein expression within duplicate pairs can be associated with the occurrence  
1689 of a phenotype in the loss-of-function mutant of the higher expressed duplicate protein implying  
1690 a dominant functional role of the more highly expressed protein. Blue arrows point out  
1691 MAC5A/MAC5B and PHB3/PHB4 as examples.

1692 e, Inference of physical protein-protein interactions from co-expression data. Distribution of pair-  
1693 wise Pearson correlation coefficients ( $R$ ) of co-expressed proteins across (at least 10) tissues  
1694 that are subunits of selected protein complexes. An  $R$  value of  $>0.5$  (shaded in grey) was  
1695 chosen as a cut-off for the selection of proteins for subsequent analysis in order to make sure  
1696 that proteins present in well characterized protein complexes are retained. CONSTITUTIVE  
1697 PHOTOMORPHOGENESIS9 SIGNALOSOME (CSN), CELLULOSE SYNTHASE (CESA).

1698 f, Recovery of annotated protein-protein interactions by co-expression analysis. Distribution of  
1699 Pearson correlation coefficients ( $R$ ) of pairs of transcripts (grey) or protein (blue) that are  
1700 annotated to interact physically in the AtPIN database<sup>33</sup> (pairs had to be detected in at least 10  
1701 matching tissues to be included in the analysis). Subsets of the AtPIN database, namely  
1702 interactions detected by the yeast two-hybrid (Y2H) method, by affinity purification - mass  
1703 spectrometry (AP-MS) or by both (Y2H+AP-MS) are displayed separately.  $R$  values  $>0.5$  are  
1704 shaded in blue (protein). Median ( $\bar{x}$ , dotted lines). The data shows that co-expression only  
1705 recovers a minority of annotated physical interactions and that interactions supported by more  
1706 than one line of experimental evidence also tend to show stronger co-expression.

1707 **Extended Data Figure 7 | Inferring protein complexes and subunit stoichiometry from**  
1708 **proteome correlation profiling using size-exclusion chromatography – mass**  
1709 **spectrometry.**

1710 a, Molecular weights of monomeric proteins (MW, determined from sequence) plotted against  
1711 the MW determined from the apex of the elution profile for proteins identified by mass  
1712 spectrometry in size-exclusion chromatography (SEC) fractions of flower tissue (sFL). The inset  
1713 shows the MW calibration of the SEC column using a protein calibration standard (MW between

1714 44 and 690 kDa). The MW distribution of proteins annotated in Araport11 is shown on top of the  
1715 scatterplot. It is apparent, that a large number of proteins show a much higher apparent MW  
1716 than what would be expected from their sequences (data points above the x=y line). This  
1717 implies that these proteins engage in physical protein interactions that are sufficiently stable  
1718 during SEC separation.

1719 b, SEC traces of proteins from five well characterized protein complexes for flower, leaf and root  
1720 tissue. Even though the resolution of SEC separations is not very high, it is apparent that the  
1721 complex subunits show very strong co-elution behaviour and that the SEC separations of the 5  
1722 complexes are reproducible between tissues. Acetyl-CoA carboxylase n = 4 proteins; Cell  
1723 division control protein 48 (CDC48) n = 3 proteins; Ribulose biphosphate carboxylase  
1724 oxygenase (RubisCO) n = 4 proteins; Prefoldin n = 6 proteins; Succinate-CoA synthetase (SCS)  
1725 n = 3 proteins.

1726 c, Intensity normalized SEC elution profile of proteins for flower tissue. Proteins are ordered  
1727 based on the SEC fraction in which their intensity peaks and the data is displayed as heat map  
1728 (n = 2,485 protein traces). Co-eluting proteins were grouped into so-called trace modules (see  
1729 methods for details). Proteins in trace modules may represent members of protein complexes  
1730 and thus serve as candidates for further experimental validation.

1731 d, In order to quantify how well protein complexes can be detected using co-expression analysis  
1732 from data in the tissue atlas (TA) or by SEC-MS a summary statistic termed 'complex index' was  
1733 calculated (see methods). The complex index is 1, when all subunits of a complex are identified  
1734 in the same module and no other proteins are contained in the module. The bar plots show  
1735 examples for complex indices obtained from the different data sets and are divided into large  
1736 (>4 subunits) and small ( $\leq 4$  subunits) protein complexes (according to UniProt). The data shows  
1737 that co-expression alone generates many candidates of interactors but that combining co-  
1738 expression and SEC-MS analysis is an efficient way to prioritize candidates for follow-up  
1739 experiments.

1740 e, Subunit heterogeneity within the coatomer complex. The coatomer complex consists of 7  
1741 subunits, five of which ( $\alpha$ ,  $\beta$ ,  $\beta'$ ,  $\epsilon$  and  $\zeta$ ) can be provided by 12 paralogs of these 5 genes. The  
1742 plots show the protein proportions of these paralogs in all 30 tissues (data from tissue atlas).  
1743 The data implies that the coatomer complex has a similar composition in most tissues. A  
1744 notable exception are seed tissues in which subunit  $\zeta$ -1 protein expression dominates over the  
1745 two other paralogous proteins suggesting that the coatomer complex in seed tissue also  
1746 preferentially contains the  $\zeta$ -1 subunit. Tissues are coloured as in Figure 1.

1747 f, Absolute SEC intensity traces of individual complex subunits for determining subunit  
1748 stoichiometry. Examples from left to right: the chaperonin complex (flower, 8 proteins, ratio of all  
1749 subunits: 1:1), the 26S proteasome core and lid (flower, 14+17 proteins, ratio of all subunits:  
1750 1:1), the COP9 Signalosome (flower, CSN; 8 proteins, ratio of all subunits: 1:1) and the

1751 CESA1/3/6 complex (root, 3 proteins, ratio of all subunits: 1:1). Note that CSN3 and CSN5 were  
1752 detected both as part of the CSN complex and in monomeric form.

1753 g, Upper panels: total intensity of protein complex subunits across all tissues for the complexes  
1754 shown in panel f (subunit intensities from the tissue atlas). Middle panels: Relative proportion of  
1755 the complex subunits within each tissue. Lower panels: Estimation of subunit stoichiometry  
1756 using the average  $\pm$  SD (n = 30 tissues) of the proportions of subunits across tissues (see  
1757 methods). For the CESA complex, the ratios were calculated for the subunit combinations  
1758 CESA1/3/6 and CESA4/7/8. The data shows that the stoichiometries determined from the tissue  
1759 expression data are generally well aligned with the expected 1:1 ratio of subunits in these  
1760 complexes. As noted above, a substantial amount of CSN5 was detected as a monomer in the  
1761 SEC analysis and the tissue expression atlas also shows higher relative expression of this  
1762 protein compared to all other complex partners. This suggests that this protein is produced in  
1763 excess over what is required for the COP9 complex (as has been observed by others before)  
1764 and may therefore imply an additional function within the cell.

#### 1765 **Extended Data Figure 8 | Kinases, phosphatases and phosphorylation motifs.**

1766 a, Percentage of annotated kinases and phosphatases family members detected at the protein  
1767 or phosphoprotein level. Brackets denote the number of genes in each family in the Arabidopsis  
1768 genome

1769 b, Tissue-resolved combined intensity (i.e. protein expression) of families of kinases (left) and  
1770 phosphatases (right). Tissues are coloured as in Figure 1. Note that several tissues (notably  
1771 pollen) stand out in terms of the expression of kinases and phosphatases implying that these  
1772 tissues are particularly active in phosphorylation-mediated dynamic signalling.

1773 c, Upper panel: Pie chart of protein expression specificity categories (see methods for definition)  
1774 for kinases and phosphatases. Lower panels: Distribution of tissue-enhanced kinases and  
1775 phosphatases across the 30 tissues showing that several tissues (notably pollen) stand out in  
1776 terms of the expression of certain kinases and phosphatases implying tissue-specific signalling.

1777 d, Pie charts showing the proportion of 'proline-directed', 'acidic', 'basic' and 'other' motif  
1778 categories for phosphorylated serine (pS), threonine (pT) and tyrosine (pY) residues. Only class  
1779 I p-sites (localization score > 0.75, methods) were considered in this analysis.

1780 e, Example motif logo plots for 'proline-directed', 'acidic', 'basic' and 'other' motifs. P-site motifs  
1781 were identified using the motif-X algorithm (see Supplementary Table 2 for all 266 motifs). n  
1782 denotes the number of phosphorylation sites that contain the respective motif; fc denotes the  
1783 fold change (i. e. enrichment) of the motif in phosphorylated vs unmodified peptides (see  
1784 methods).

1785 f, Enrichment of 'proline-directed' (yellow), 'acidic' (red), 'basic' (blue) and 'other' (grey)  
1786 sequence motifs (circles) in the serine p-site dataset versus the same motifs detected in the  
1787 background dataset of unmodified peptides (see methods). Motifs are shown for 2, 3 and 4 fixed  
1788 amino acid positions. The p-site in each motif example is underlined. X denotes any amino acid.

1789 g, Number of identified p-sites for a given protein plotted against the sequence lengths of the  
1790 same protein. LATE EMBRYOGENESIS ABUNDANT (LEA) proteins are marked by a circle and  
1791 arrow.

1792 h, Schematic representation of the LEA protein sequences (black bars). Pink marks denote  
1793 phosphorylated and blue marks unphosphorylated STY residues. It is evident, that almost all  
1794 STY residues in LEA proteins can be phosphorylated.

1795 i, Schematic representation the sequences and domain topology of the receptor-like kinases  
1796 STRUBBELIG RECEPTOR FAMILY4 (SRF4), FERONIA (FER) and CHITIN RECEPTOR  
1797 KINASE1 (CERK1). It is apparent that p-sites often preferentially occur in specific domains,  
1798 notably the juxtamembrane domain. Protein sequence regions covered by identified peptides  
1799 are marked in blue and p-sites are marked in pink.

1800 **Extended Data Figure 9 | Functional analysis of phosphorylation mutants of RCAR10 and**  
1801 **QKY.**

1802 a, Phosphorylation site (p-site) localization within the structure of REGULATORY  
1803 COMPONENTS OF ABA RECEPTOR10 (RCAR10). The RCAR10 structure (blue) was  
1804 modelled using the RCAR11 protein crystal structure (cornflowerblue) as a template <sup>45</sup>. ABA-  
1805 binding loops are shown in turquoise, p-sites in pink and ABA ligand in yellow.

1806 b, RCAR10 expression across tissues at the protein (blue, iBAQ), transcript (grey, TPM) and p-  
1807 site (pink, intensity) level.

1808 c, Tissue-resolved total protein intensity and relative proportions of the members of the protein  
1809 phosphatase 2C (PP2C) co-receptor family. Note that seed tissues stand out in terms of overall  
1810 expression as well as the dominance of AHG1 in these tissues.

1811 d, Measurement of ABA response when expressing RCAR or RCAR10 phosphomimetic mutant  
1812 variants in combination with different PP2C co-receptors in protoplasts (see methods). Columns  
1813 display the average ABA response ( $\pm$ SD, n = 3) and grey dots indicate individual  
1814 measurements. The data shows that co-expression of the phosphatases HAI1-3 lead to similar  
1815 responses of the phosphomimetic mutants, whereas other co-expressed phosphatases show  
1816 diverse responses.

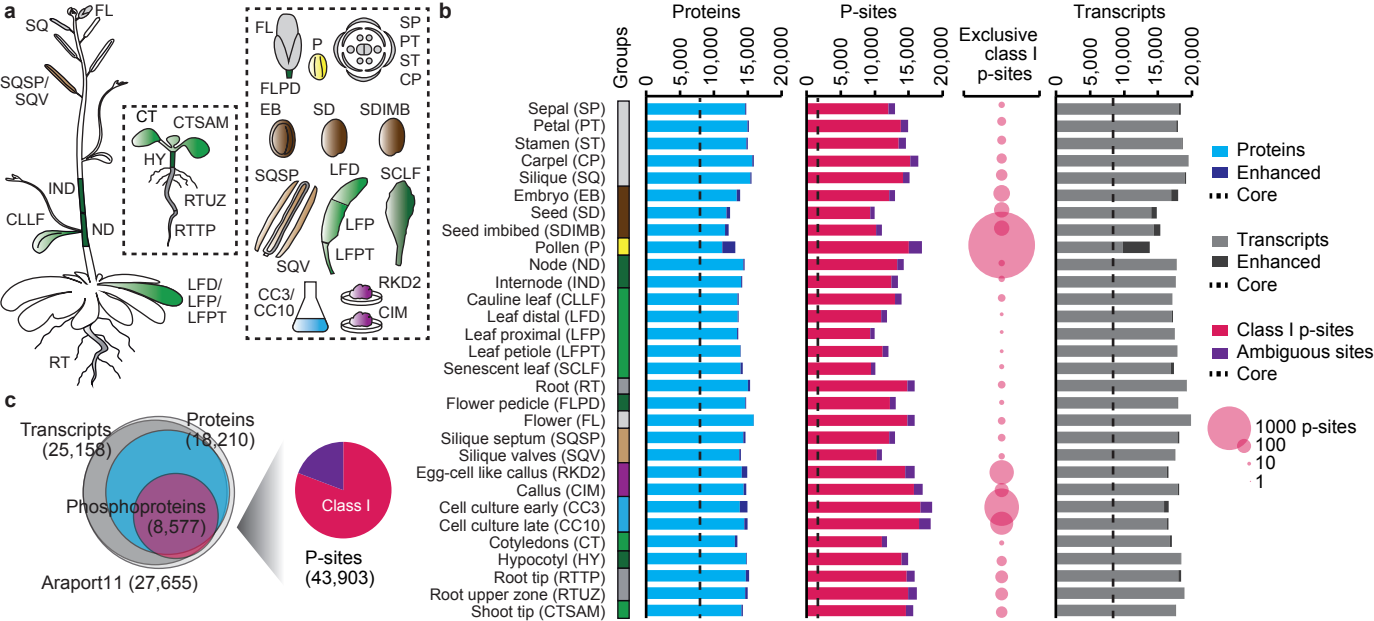
1817 e, QUIRKY (QKY) expression across tissues at the protein (blue, iBAQ), transcript (grey, TPM)  
1818 and p-site (pink, intensity) level.

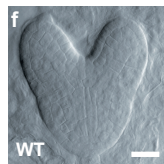
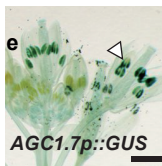
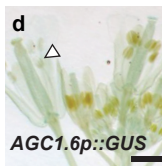
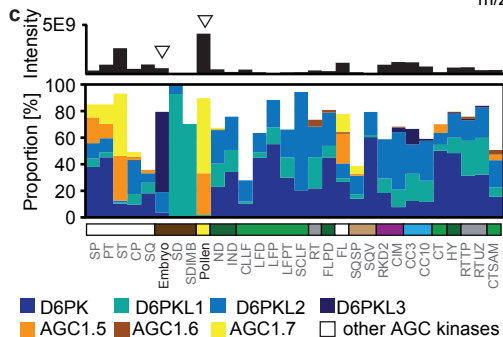
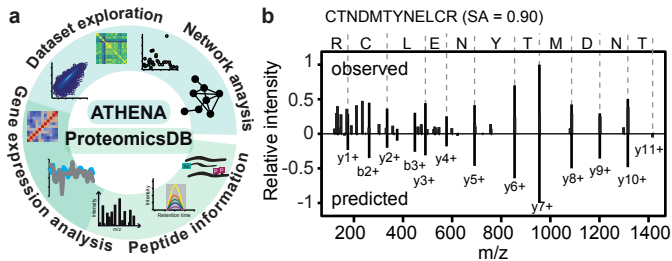
1819 f, Members of the MULTIPLE C2 AND TRANSMEMBRANE DOMAIN-CONTAINING PROTEIN  
1820 (MCTP) family clustered by sequence similarity (left) and schematic representation of their  
1821 domain structures along with detected p-sites (right). MCTP11a, 12 and 13 were not detected in  
1822 this study (n.d.). QKY (MCTP15) is marked in bold.

1823 g, Number of independent transgenic plant lines (*qky-9* mutant background) transformed with  
1824 WT (QKY), phosphomutant (SA) or phosphomimic (SE) constructs that show complete, partial  
1825 or no rescue of the mutant phenotype. qPCR results (average  $\pm$  SD; individual data points as  
1826 grey dots) show the relative transgene expression in wild type (WT), *qky-9* mutant and selected  
1827 transgenic lines. QKY wild type (grey), QKY<sub>S262A</sub> (SA; blue), QKY<sub>S262E</sub> (SE, purple).

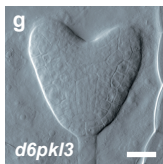
1828 h-j, Representative confocal images of six days-old *qky-9 pQKY::mCherry:QKY* (WT QKY; n =  
1829 14 roots), *qky-9 pQKY::mCherry:QKYS262A* (phosphomutant; n = 21 roots), *qky-9*  
1830 *pQKY::mCherry:QKYS262E* (phosphomimic; n = 15 roots) root epidermal cells of the  
1831 meristematic zone. The punctate signal along the cell circumference shows the expected  
1832 localization of QKY protein. Arrows indicate punctate structures. Scale bars 5  $\mu$ m.



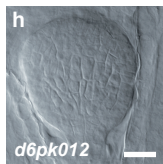




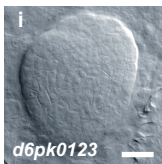
87% (n = 28)



97% (n = 67)



31% (n = 52)



71% (n = 44)

